NEUTRON SCATTERING STUDIES OF THE FRUSTRATED ANTIFERROMAGNETIC PYROCHLORE SYSTEM $\mathbf{Tb_2Sn_{2-x}Ti_xO_7}$

NEUTRON SCATTERING STUDIES OF THE FRUSTRATED ANTIFERROMAGNETIC PYROCHLORE SYSTEM $Tb_2Sn_{2-x}Ti_xO_7$

By

JIMIN ZHANG, B.Sc.

A Thesis

Submitted to the School of Graduate Studies

in Partial Fulfilment of the Requirements

for the Degree

Master of Science

McMaster University

MASTER OF SCIENCE (2013) McMaster University
(Physics and Astronomy) Hamilton, Ontario

TITLE: Neutron Scattering Studies of the Frustrated Antiferromagnetic Pyrochlore System $Tb_2Sn_{2-x}Ti_xO_7$

AUTHOR: Jimin Zhang, B.Sc.

SUPERVISOR: Professor Bruce. D. Gaulin.

NUMBER OF PAGES: xv, 88

Abstract

The following dissertation shows the results of a series of inelastic neutron scattering experiments on the geometrically frustrated pyrochlore system $\mathrm{Tb_2Sn_{2-x}Ti_xO_7}$ for x=0, 0.1, 0.2, 0.5, 1, 1.5 and 2. Inelastic neutron scattering measurements were performed on the SEQUOIA direct geometry time-of-flight spectrometer at the Spallation Neutron Source of Oak Ridge National Laboratory. For the two end members, x=0, $\mathrm{Tb_2Sn_2O_7}$ and x=2, $\mathrm{Tb_2Ti_2O_7}$, they display related, but different exotic ground states, with $\mathrm{Tb_2Sn_2O_7}$ displaying "soft" spin ice order below $\mathrm{T_N}{\sim}0.87\ \mathrm{K}$, while $\mathrm{Tb_2Ti_2O_7}$ enters a glassy antiferromagnetic spin ice state below $\mathrm{T_g}{\sim}0.2\ \mathrm{K}$.

The first two chapters give a brief introduction to the physics of geometrically frustrated magnetism and neutron scattering. Chapter 3 studies the two end members $\mathrm{Tb_2Ti_2O_7}$ and $\mathrm{Tb_2Sn_2O_7}$ experimentally and theoretically. Inelastic neutron scattering measurements and appropriate crystal field calculations together probe the crystal field states associated with the J=6 states of $\mathrm{Tb^{3+}}$ within the appropriate $\mathrm{Fd\bar{3}m}$ pyrochlore environment. These crystal field states determine the size and anisotropy of the $\mathrm{Tb^{3+}}$ magnetic moment in each material's ground state, information that is an essential starting point for any description of the low temperature phase behavior and spin dynamics in $\mathrm{Tb_2Ti_2O_7}$ and $\mathrm{Tb_2Sn_2O_7}$. Chapter 4 treats neutron scattering, as well as accompanying AC magnetic susceptibility and μSR measurements performed by our collaborators on a series of solid solutions $\mathrm{Tb_2Sn_{2-x}Ti_xO_7}$ showing a novel, dynamic spin liquid state for all x other than the end members x=0 and x=2. This state is the result of disorder in the low lying $\mathrm{Tb^{3+}}$ crystal field environments which de-stabilizes the mechanism by which quantum fluctuations contribute to ground state selection in $\mathrm{Tb_2Sn_{2-x}Ti_xO_7}$.

Acknowledgement

My deepest gratitude goes first and foremost to my supervisor, Professor Bruce Gaulin. First of all, I would like to thank him for accepting my Master application two years ago. As an international Chinese student who is not fluent in English, I want to express my sincere appreciation to him for his trust and constant encouragement during the two-year study. Then, I would like to thank Bruce for his instructive advice and useful suggestions on my research and thesis. This is really a very good project and I am deeply grateful of his help in the completion of this thesis. I am very proud to have such a nice supervisor. Working with Bruce will give me wonderful memories in future.

I must thank all the students in my group, Katharina Fritsch, Jerod Wagman, Kate Ross, Dalini Maharaj, Edwin Kermarrec, and Makoto Tachibana. We are a large and warm family. Special thanks should go to Katharina who helped and taught me a lot in my study.

During this project, I also benefitted from many useful discussions and helpful suggestions from Prof. Michel Gingras and his student Zhihao Hao at University of Waterloo and here I would like to thank them.

I of course also want to acknowledge all the collaborators in the experiment work in this thesis. I wish to thank Prof. Cava’s group in the Department of Chemistry at Princeton University for the synthesis of the samples, and I also want to thank our experimental collaborators, Philippe Mendels’s and Fabrice Bert’s groups and Peter Schiffer’s group who provided the μSR data and AC magnetic susceptibility data respectively.

I would also like to thank all the faculty, staff and graduate students at the Department of Physics and Astronomy as well as all the friends I met in

McMaster University for their help in this time. I would also like to acknowledge the generous financial support by McMaster University and NSERC of Canada.

Finally, I am indebted to my beloved parents for their unlimited support all through the four years when I came to Canada alone to study.

Table of Contents

List of Figures

List of Tables

Chapter 1

Introduction

1.1 Introduction

Magnetic materials are very common in the world. Many magnetic materials exhibit varied and interesting physical properties. For such materials, some of the atoms in the crystalline solid have nonzero magnetic moments which originate from the intrinsic magnetic moment (or spin) and orbital angular momentum of the unpaired electrons residing in the atom. People have studied magnetic materials theoretically and experimentally for a long time. In Chapter 2, I will introduce one experimental technique, — neutron scattering, which is used to investigate the magnetic properties of the magnets we are interested in. In this chapter, I will discuss some background and general behavior of the type of magnet studied in this thesis. Firstly, I will talk about some concepts of magnetism in general. Next, I will introduce the concept of geometrical frustration as manifested in one of the canonical families of the three dimensionally geometrically frustrated magnets -- the pyrochlore lattice. Then, I will talk about crystal field effects in the specific terbium-based pyrochlore system as well as the crystal field calculation which is the main theoretical result in this thesis. Finally, I will introduce two isostructural pyrochlore magnets, $\mathrm{Tb_2Ti_2O_7}$ and $\mathrm{Tb_2Sn_2O_7}$, which are the main focus of study in this thesis.

1.2 Magnetism

Let's start from a simple Heisenberg model to describe two interacting magnetic moments on different ions: [1]

$$\hat{H} = -\sum_{ij} J_{ij} \mathbf{S}_i \cdot \mathbf{S}_j \tag{1.1}$$

where J_{ij} is the exchange constant between spin S_i and spin S_j and the sum is over each pair of spins in the system. At low temperatures, in order to get a low internal energy, a pair of spins prefers to point in parallel directions for $J_{ij}>0$, while the pair prefers to point in anti-parallel directions for $J_{ij}<0$. These two cases are called ferromagnetism (FM) and antiferromagnetism (AFM) respectively. At high temperatures, in order to minimize the free energy, the entropy must be maximized in the system, which means the system enters a disordered state, known as paramagnetism. In the extreme version of this state, all the spins point in all the possible directions with equal probability at any time. There exists a critical temperature T_C at which a phase transition occurs between an ordered phase (FM or AFM) if it exists, and a disordered phase (paramagnetism). This kind of phase transition can be either continuous or second order, or discontinuous or first order [2,3]. A quantity called the order parameter is zero above T_C and non-zero below T_C. In the case of a simple magnetic phase transition, the order parameter is the magnetization, m, or the sublattice magnetization. In the paramagnetic phase, $m=<S>=0$, while in ordered phase, $m=<S>\neq 0$. Therefore, the order parameter m increases from zero to non-zero when the temperature drops through the critical point T_C.

1.3 Geometrical Frustration

Let’s now consider a simple example of an Ising model on a square lattice (Fig.1.1 a). In the Ising model, the spins can only point along one direction which is usually named as the $\pm\hat{z}$ easy-axis. The four Ising spins on the corner of a square lattice with antiferromagnetic nearest neighbor interactions orient in an anti-parallel configuration with their neighbors at low temperature in the ground state. Therefore, the ground state is an ordered antiferromagnetic structure. However, if the geometry changes to a triangular one in two dimensions, quite a different ground state behavior occurs and no magnetic phase transition exists at any temperature.

Figure 1.1 b shows three spins with antiferromagnetic near neighbor interactions residing on the corners of a triangle. If two of the three spins align anti-parallel, the third one cannot decide to point up or down because it is impossible to satisfy all the pair-wise spin interactions simultaneously [4]. Therefore, the ground state of such system is frustrated with a highly degeneracy because of the special geometry. In a single triangle, the ground state is six fold degenerate with any two spins up and the other one down. By adding more triangles together to build up a triangular lattice [5,6] or a kagome lattice [7-10], the number of degenerate ground states increases and there is no transition to an ordered state at zero temperature [11].

Such a simple example helps us introduce the concept of geometrical frustration [12, 13]. In such a system, the minimum energy of the system does not correspond to the minimum energy of all the pair-wise interactions and there is an incompatibility between the lattice geometry and the interactions. Therefore, the system cannot find a unique ordered ground state and there is no phase transition to a magnetic long range order at any temperature.

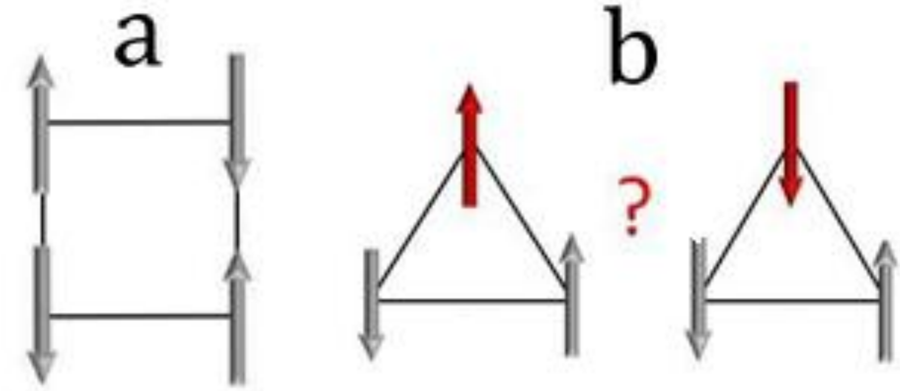

Figure 1.1: a. Four Ising spins on the corners of a square with antiferromagnetic interaction can form an antiferromagnetic ordered structure. b. Three Ising spins with antiferromagnetic interaction on a triangle is frustrated because only two of the three spins can align anti-parallel but the third one cannot minimize the interactions with two neighbors simultaneously [4].

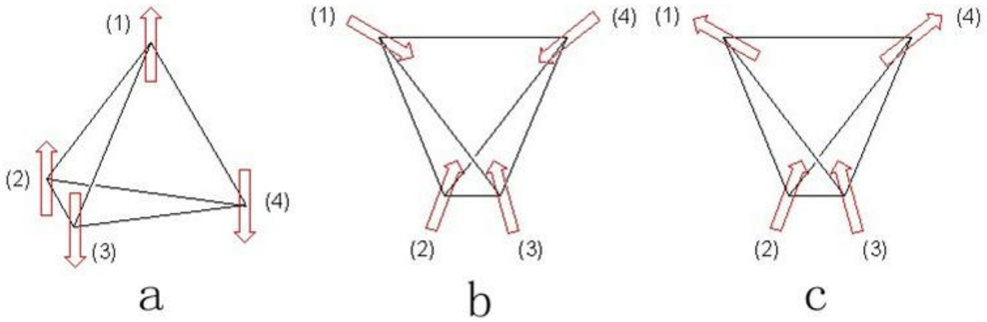

Figure 1.2: a. Ground state of collinear AFM Ising spins in a tetrahedron. b. Ground state of AFM <111> Ising spins in a tetrahedron. c. Ground state of FM <111> Ising spins in a tetrahedron.

The triangle geometry is a two dimensional case of geometrical frustration. Of course, there exists a three dimensional version of geometrical frustration. That is tetrahedral geometry with four antiferromagnetic spins residing on the four vertices of a tetrahedron.

As in the triangle case, the four collinear Ising spins with antiferromagnetic interactions cannot minimize all the interaction energies simultaneously and the system is frustrated [14]. As shown in Figure 1.2 a, the ground state of such a system is a two up/two down configuration with six fold degeneracy. Again, by adding more tetrahedra together to build up a pyrochlore lattice, the degeneracy of the ground state increases.

So far, we have considered collinear configurations for which only antiferromagnetic interactions can lead to frustration. Now, we have to consider more complicated (than Ising) anisotropy because it plays an important role in the physics of geometrical frustration. The combination of the magnetic moment's interactions and anisotropies and certain lattice geometries leads to the system having difficulty ordering conventionally at low temperatures [15,16]. In the presence of strong single-ion anisotropy, even ferromagnetic interactions can result in frustration. Let us focus on the pyrochlore lattice. With a more general spin anisotropy, the spin is no longer in the collinear up/down configuration, but it can point into or out of the centre of the tetrahedron, for example. This is known as local <111> anisotropy. In the case of AFM <111> Ising spins pyrochlore, the ground state is an all-in/all-out doublet ordered state (Fig. 1.2 b), which is quite different from the collinear Ising spin case. In the case of FM <111> Ising spins on the pyrochlore lattice, the ground state is a six fold degenerate two-in/two-out disordered state, which is the well known spin ice state (Fig. 1.2 c), an analogue to the structure of water ice [17]. Independent of whether the system is 2D or 3D, magnetism on geometrically frustrated lattices often leads to exotic ground states which may lack long-range order, such as spin glass [18-22], spin liquid [23-25], and spin ice states [26-30].

1.4 The Pyrochlore Lattice

The phenomenon of geometrical frustration on cubic pyrochlore lattices is what we consider in this thesis. We will focus on the pyrochlore structure with chemical formula of $\mathrm{R_2M_2O_7}$, crystallizing into the face centered cubic structure and space group $\mathrm{Fd\bar{3}m}$. R is a trivalent rare earth magnetic ion (e.g. $\mathrm{Gd^{3+}, Tb^{3+}}$, $\mathrm{Yb^{3+}}$, $\mathrm{Er^{3+}}$, $\mathrm{Dy^{3+}}$ and $\mathrm{Ho^{3+}}$) with eightfold oxygen coordination, forming a sublattice of a network of corner-sharing tetrahedra. M can be either a tetravalent nonmagnetic ($\mathrm{Ti^{4+}, Zr^{4+}, Sn^{4+}}$) or a magnetic ($\mathrm{Mn^{4+}, Mo^{4+}}$) transition metal ion with sixfold oxygen coordination, forming another sublattice of a network of corner-sharing tetrahedra. The two sublattices of R ions and M ions are independent and interpenetrating to each other [31]. Here, we only focus on those cubic pyrochlores for which only the R sublattice is magnetic and the M sublattice is nonmagnetic. Since the nonmagnetic ion M does not contribute to the magnetic properties of the system, we will concentrate on the properties of the R ion and the crystal field effect on the R ion induced by its local oxygen environment. As we discussed previously, the exotic ground state is governed by the interplay between exchange and dipolar interactions between the R magnetic ions and the crystal field induced single ion anisotropy [26]. The exchange interactions between magnetic moments depend on the overlap of magnetic and nonmagnetic orbitals and are thus independent of the size of the moments involved, but the dipolar interactions follow directly from the size of the moments and the geometry of the sublattice on which they reside. These dipolar interactions tend to be significant in the $R_2M_2O_7$ pyrochlores, as the R^{3+} moments tend to be large [31]. Moreover, for the M site, different M ions can affect the lattice size as well as the oxygen environment surrounding R ions, which also give rise to a significant difference in the magnetic behavior of the system.

In this thesis, we will focus on a series of pyrochlore solid solutions $Tb_2Sn_{2-x}Ti_xO_7$ and study the low temperature magnetic behaviour, the crystal field states and the phase behaviour across the solid solution from one end member, $Tb_2Ti_2O_7$, to the other end, $Tb_2Sn_2O_7$. For the remainder of this chapter, I will introduce the crystal field effect on the terbium (Tb^{3+}) pyrochlores as well as the associated crystal field calculation. In the end, I will summarize some of the important background knowledge of $Tb_2Ti_2O_7$ and $Tb_2Sn_2O_7$ which has been uncovered to date.

1.5 Crystal Field Effects in Terbium Pyrochlores

The electrostatic interaction between the electrons of a magnetic ion and its crystalline environment can lift the (2J+1)-fold degeneracy of the magnetic levels determined by Hund’s rules for a particular electronic configuration. The general form of the lifting of the degeneracy depends on the point symmetry of the magnetic ion within the crystal structure. In the case of Tb^{3+}, the Tb^{3+} ion possesses 8 electrons in its 4f shell and Hund’s rules tell us **L**=3, **S**=3 and **J**=**L**+**S**=6 corresponding to a $^7F_6$ magnetic ion. The 4f-electrons in Tb^{3+} interact with the oxygen environment surrounding each Tb^{3+} so as to determine the single ion properties of Tb^{3+} as well as the crystal field levels of Tb^{3+} in the pyrochlore lattices.

Now, let’s consider the oxygen environment around each Tb^{3+} ion (Fig.1.3). In the case of $Tb_2M_2O_7$ which crystallizes into the $Fd\bar{3}m$ space group, the local chemical environment of each Tb^{3+} (blue) consists of eight oxygen anions which form a distorted cube. Two (green) of the eight oxygens making up this cube, lie along the diagonal of the cube (the local <111> direction), and are closer to the Tb^{3+} ion than are the other six (red), roughly coplanar oxygen ions. These six oxygen ions form a distorted ring normal to the local <111> direction [32]. Therefore, the local crystal field at the Tb^{3+} site has D_{3d} symmetry. Changing the non-magnetic ion sites, M, would affect the distance of the six red oxygens from the Tb^{3+} site. Therefore, different terbium pyrochlores would have different configurations of the oxygen environment, resulting in the different crystal field effects and crystal field states of Tb^{3+}.

In Tb^{3+} with a partially filled 4f-electrons shell, the spin-orbit coupling is strong and the electrostatic interactions between the 4f electrons in Tb^{3+} and the crystal environment are weaker than the spin-orbit interaction. Therefore, the total angular momentum **J** can be taken as a good quantum number to describe the magnetic moment. In the case of Tb^{3+} with **J**=6, the single ion ground state would form a 2J+1=13 fold degenerate multiplet assuming there is no external perturbation. However, the degeneracy is lifted when the single ion Tb^{3+} interacts with the distorted cubic oxygen environment and the crystal electric field forces the magnetic moments to point along the cubic distortion direction (i.e. the local <111> direction) inducing an Ising-like local <111> anisotropy. As a result, the 2J+1=13 levels split into the energy eigenstates of the crystal field. The energies and wavefunctions of these crystal field levels determine the size and anisotropy of the magnetic moments of the Tb^{3+} ions, as well as their interactions at low temperature.

By using the point charge approximation [32,33], we can derive the crystal field Hamiltonian in terms of Stevens operators, O_n^m, which are functions of the total angular momentum $(J, J_z, J_+ \text{ and } J_-)$ [34]. Figure 1.3 shows the local

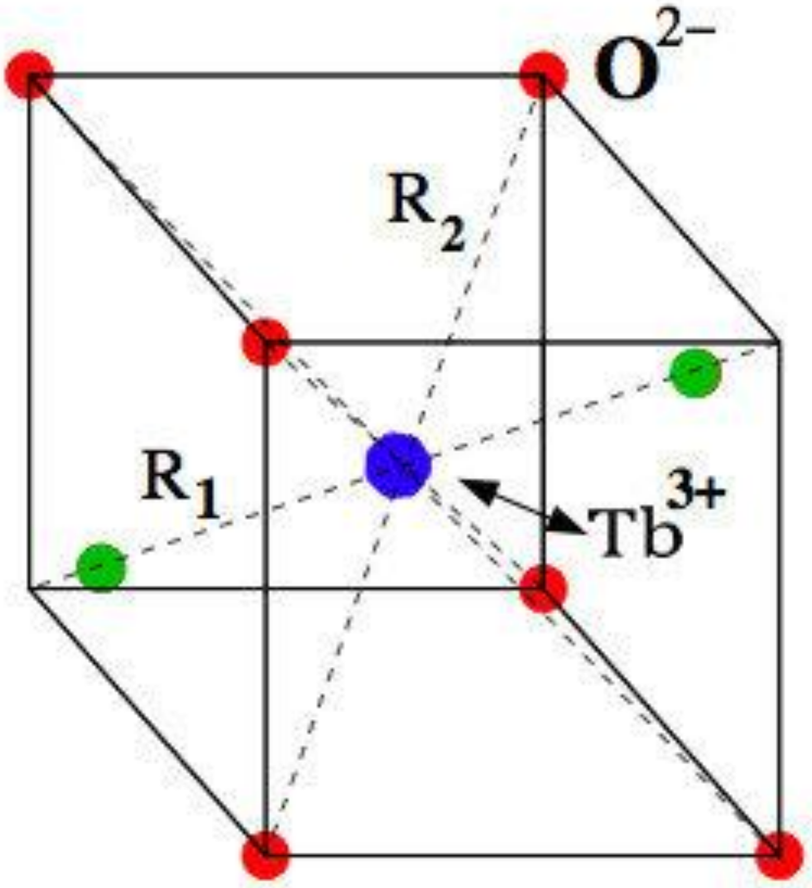

Figure 1.3: The crystal environment immediately around the Tb^{3+} ion (blue in the centre) within $Tb_2M_2O_7$. Tb^{3+} is surrounded by eight oxygens (red and green in the vertices of the cube) which comprise a distorted cube. The two apical oxygens (green) along one diagonal of the cube (the local <111> directions) are closer to the Tb^{3+} ion than are the other six oxygens (shown in red).

environment at the Tb^{3+} site in $Tb_2M_2O_7$, M=Ti and Sn, and the threefold rotational symmetry about one of the cube diagonals, the local <111> direction. As a result, the crystal field Hamiltonian is invariant under three fold rotations around the local <111> direction as well as point inversion with respect to Tb^{3+} site. Taking into account these constraints, the crystal field Hamiltonian for Tb^{3+} in $Tb_2M_2O_7$ can be written as [32, 35, 36]:

$$H_{cf} = \alpha_J D_2^0 O_2^0 + \beta_J (D_4^0 O_4^0 + D_4^3 O_4^3) + \gamma_J (D_6^0 D_6^0 + D_6^3 O_6^3 + D_6^6 O_6^6), \qquad (1.2)$$

where the coefficients are α_J=-1/99, β_J=2/16335, γ_J=-1/891891 for Tb^{3+}, O_n^m are Stevens operators, and D_n^m are crystal field parameters that have to be determined experimentally for different terbium pyrochlores [36]. Since only **J** is the good quantum number here, the eigenstates of the total angular momentum **J** are good states. Therefore, we calculate the crystal field Hamiltonian in the $|J,\ J_z>$ basis [33].

Here, I have to emphasize that the crystal field states of the crystal field Hamiltonian in the basis states $|J,\ J_z>$ are written in the local <111> basis. For an arbitrary tetrahedron placed in the global basis, the four Tb^{3+} sites have their own local <111> basis which have different transformation relations relative to the global basis. Therefore, we must find the transformation relation between the global basis and the local basis for the four Tb^{3+} sites in a tetrahedron. This is important because when we calculate the magnetic neutron scattering cross section in chapter 3, the matrix elements of the **J** operators in the equation is in the global basis and we have to make sure the **J** operator and the $|J,\ J_z>$ basis are compatible. The transformation relation between the global axis frame and the local axis frame for the four Tb^{3+} sites in a given tetrahedron is given below:

$$x_1' = \frac{1}{\sqrt{6}}(-x - y + 2z), \quad y_1' = \frac{1}{\sqrt{2}}(x - y), \quad z_1' = \frac{1}{\sqrt{3}}(x + y + z);$$

$$x_2' = \frac{1}{\sqrt{6}}(x + y + 2z), \quad y_2' = \frac{1}{\sqrt{2}}(-x + y), \quad z_2' = \frac{1}{\sqrt{3}}(-x - y + z);$$

$$x_3' = \frac{1}{\sqrt{6}}(-x + y - 2z), \quad y_3' = \frac{1}{\sqrt{2}}(x + y), \quad z_3' = \frac{1}{\sqrt{3}}(x - y - z);$$

$$x_4' = \frac{1}{\sqrt{6}}(x - y - 2z), \quad y_4' = \frac{1}{\sqrt{2}}(-x - y), \quad z_4' = \frac{1}{\sqrt{3}}(-x + y - z); \qquad (1.3)$$

where x, y, z are the global axis and x’, y’, z’ are the local axis.

The crystal field Hamiltonian contains the $O_2^0, O_4^0, O_4^3, O_6^0, O_6^3$ and O_6^6 Stevens operators. Among them, when acting on |J, J_z>, only |J, J_z> will appear for O_n^0 (i.e. only diagonal matrix elements appear), and only $|\, J,\ J_z \pm 3>$ and $|\, J,\ J_z \pm 6>$ will appear for O_n^3 and O_6^6 respectively. Therefore, the crystal field Hamiltonian (Equation 1.2) has a certain symmetry which gives rise to all the eigenstates being of the structure $|\Phi >= \sum_n Cn|J = 6,\ Jz = m \pm 3n>(Jz \leq J)$. Therefore, if we look at the eigenstates of the ground state doublet of Tb^{3+} in pyrochlore system, we can find m=±4 and the doublet states consists of only |6, ±4>, |6, ±1>, |6, ∓2> and |6, ∓5> basis states. This conclusion is consistent with the results of ground state doublet eigenstates of $Tb_2Ti_2O_7$ and $Tb_2Sn_2O_7$ in Chapter 3.

In some references, work is performed within another equivalent formalism of the crystal field Hamiltonian expressed in terms of spherical harmonics:

$$H'_{cf} = \sum_{nm} B_n^m \sqrt{\frac{4\pi}{2n+1}}\, Y_n^m \qquad (1.4)$$

where B_n^m are also called crystal field parameters. The two sets of coefficients D_n^m and B_n^m in Equation 1.2 and Equation 1.4 can be transformed into each other by $D_n^m = \lambda_n^m B_n^m$, where λ_n^m are given for Tb^{3+} in Table 1.1 [35].

The crystal field parameters are difficult to calculate from first principles, so they are usually determined by comparison between theoretical crystal field calculations and experimental data. The most direct comparison is to inelastic

Table 1.1. Values of λ_n^m for Tb^{3+}

λ_2^0	λ_4^0	λ_4^3	λ_6^0	λ_6^3	λ_6^6
1/2	1/8	$-\sqrt{35}/2$	1/16	$-\sqrt{105}/8$	$\sqrt{231}/16$

neutron scattering data, as this technique directly probes the spectroscopy of the crystal field eigenfunctions, according to dipole selection rules. This is one reason why we performed the neutron scattering measurements on $\mathrm{Tb_2Ti_2O_7}$ and $\mathrm{Tb_2Sn_2O_7}$, and this work is described in Chapter 3.

1.6 Quantum Spin Ice $\mathbf{Tb_2Ti_2O_7}$

In this section, we present an introduction to $\mathrm{Tb_2Ti_2O_7}$, whose properties have been debated for almost 15 years. It displays a well known spin liquid ground state characterized by the absence of magnetic long range order down to 50mK [23,24] and remains dynamic with short range correlations, of the order of nearest neighbor distance, between fluctuating spins. The Θ_{CW}~-19 K [23,24,35] Curie-Weiss temperature implies an antiferromagnetic exchange interaction between spins. The net interaction is antiferromagnetic arising from the near neighbor antiferromagnetic exchange interaction being stronger than the comparable near neighbor ferromagnetic dipole interaction. Meanwhile, the local <111> Ising-like spins resulting from the crystal field within the ground state doublet puts $\mathrm{Tb_2Ti_2O_7}$ in the configuration of the AFM <111> Ising model, which should favor an all-in/all-out ordered phase on the pyrochlore lattice [37], as we previously explained. Theoretically, for given dipole and exchange interactions appropriate to $\mathrm{Tb_2Ti_2O_7}$, Monte Carlo simulations predict a magnetic phase transition at about 1.2 K [26], which is inconsistent with the experimental results. $Tb_2Ti_2O_7$ does show evidence for a spin glass state at temperatures below ~0.2 K [25,38-40], and there has been a flurry of recent neutron scattering work, showing evidence for both "pinch point" diffuse scattering and short range frozen order with a (1/2,1/2,1/2) ordering wavevector, also at temperatures of ~0.2 K [41,42]. The quasi-Bragg peaks observed at the (1/2,1/2,1/2) ordering wavevectors have been modeled on the basis of an antiferromagnetically correlated "soft" spin ice state, where all spins within a cubic unit cell point either into or out of the tetrahedra on which they reside, locally satisfying the two spins in - two spins out, "ice rule" [41]. However, neighboring cubic unit cells are π out of phase with respect to each other, and the resulting order extends only over a couple of unit cells. The "soft" descriptor here refers to the fact that the spins do not point along local <111> directions. That is, they do not point exactly into or out of the tetrahedra, but make an angle of ~12° with respect to their local <111>.

An important question is: why is $Tb_2Ti_2O_7$ frustrated at low temperature and what is the origin of its spin liquid ground state? Two theoretical proposals have been put forward to explain why $Tb_2Ti_2O_7$ fails to order at temperatures ~1.2 K, both of which critically involve the crystal field eigenfunctions and eigenvalues for Tb^{3+} in $Tb_2Ti_2O_7$. One of these is referred to as "quantum spin ice" ground state. Theoretical analysis found that $Tb_2Ti_2O_7$ is very close to the boundary of the all-in/all-out ordered state and two-in/two-out disordered spin ice state, implying that a small perturbation can move it to the disordered spin ice phase. Unlike in the "classical" spin ice $Ho_2Ti_2O_7$ [27,43,44] and $Dy_2Ti_2O_7$ [45] where the gap between crystal field ground state doublet and first excited state doublet is a few hundred times larger than the exchange and dipole interactions, the Tb^{3+} crystal field energy gap between the ground state doublet and lowest lying excited state doublet is much smaller (~18K gap) [46] in $Tb_2Ti_2O_7$. Second order perturbation theory allows a virtual crystal field excitations between the ground state doublet and first excited state doublet, which can renormalize the effective interactions between the nearest neighbor moments from antiferromagnetic to ferromagnetic and move $Tb_2Ti_2O_7$ to the frustrated spin ice phase, precluding conventional order [41, 47]. This virtual excitation also plays a major role in the spin fluctuation spectrum since the mixing with higher crystal field states tends to restore transverse spin components. Because of these strong quantum effects, $Tb_2Ti_2O_7$ and other such quantum pyrochlore magnets are expected to be governed by a more complicated expression of nearest neighbor exchange Hamiltonian than that of Equation 1.1: [48]

$$H = \frac{1}{2}\sum_{ij} J_{ij}^{\mu\nu} S_i^{\mu} S_j^{\nu} =$$

$$\sum_{<ij>}\{J_{zz} S_i^z S_j^z - J_{\pm}(S_i^+ S_j^- + S_i^- S_j^+) + J_{\pm\pm}(\gamma_{ij} S_i^+ S_j^+ + \gamma_{ij}^* S_i^- S_j^-) +$$

$$J_{z\pm}[(S_i^z(\zeta_{ij} S_j^+ + \zeta_{ij}^* S_j^-) + i \leftrightarrow j]\} \qquad (1.5)$$

where S_i^{μ} are local spin coordinate. In this equation, J_{zz} is the Ising exchange constant responsible for the nearest-neighbor spin ice model, and the other three terms $J_{\pm}$, $J_{\pm\pm}$ and $J_{z\pm}$ allow quantum fluctuations. Details of this Hamiltonian can be found in reference Ross *et al.*[29].

In $Tb_2Ti_2O_7$, the ground state doublet is not protected by Kramers' theorem due to an even number of electrons in Tb^{3+}, so a competing theoretical scenario has been proposed by Bonville and collaborators. They propose that $Tb_2Ti_2O_7$ undergoes a Jahn Teller phase transition at low but finite temperature to a singlet ground state, creating a sufficiently large singlet-singlet gap such that magnetic order does not occur [49].

1.7 "Soft" Spin Ice $Tb_2Sn_2O_7$

Another material under study in this thesis is $Tb_2Sn_2O_7$ which is isostructural to $Tb_2Ti_2O_7$, formed by replacing the nonmagnetic ion Ti^{4+} with another nonmagnetic ion, Sn^{4+}. This substitution yields a lattice expansion as well as modification of the oxygen environment of Tb^{3+} site and therefore dramatically affects the balance of the interactions, the crystal field states and eventually the magnetic properties of the system. In contrast to $Tb_2Ti_2O_7$, $Tb_2Sn_2O_7$ can only be studied in polycrystalline form, due to the strong tendency of SnO_2, a starting material in its growth, to sublimate at modest temperatures. While less extensively studied than $Tb_2Ti_2O_7$ for that reason, it has also been less controversial in part because it does exhibit clear signs of magnetic order at temperatures of ~1 K. With a Cuire Weiss temperature of -12 K [50], $Tb_2Sn_2O_7$ has an antiferromagnetic near neighbor exchange interaction and a ferromagnetic dipolar interaction as well. $Tb_2Sn_2O_7$ is strongly (~3%) expanded compared with $Tb_2Ti_2O_7$, with room temperature lattice parameters of a=10.426 Å [51] and a=10.149 Å [24], respectively. The lattice expansion tends to strengthen ferromagnetic near neighbor dipolar interactions relative to antiferromagnetic exchange interactions and produces an overall ferromagnetic interaction. From neutron diffraction measurements [51], a two-step ordering process with ferromagnetic correlations appearing below ~1.3 K, followed by a phase transition to an ordered “soft” spin ice state below $T_C = 0.87$ K is observed [51,52]. The “soft” descriptor refers to the fact that the Ising crystal field anisotropy on Tb^{3+} is weak and the Tb^{3+} moments are oriented at a small angle of $13{,}3^\circ$ with respect to their local <111> directions (directly into or out of the tetrahedra) [51,53]. The two spins in, two spins out, “ice rule” is obeyed within the soft ordered spin ice structure of $Tb_2Sn_2O_7$ below T_C. It is an unusual ordered state, distinct from the disordered “classical” spin ice state by virtue of the long range correlations present within it. Despite the evidence provided for long range order by neutron scattering, μSR experiments show this ordered spin ice state to coexist with slow, correlated magnetic fluctuation on the time scale of 10^{-4} s to 10^{-8} s and which persist down to the lowest temperature [52, 54].

Bibliography

1. Magnetism in Condesed Matter, Stephen Blundell (Oxford University Press, 2001)

2. Introduction to modern statistical mechanics, David Chandler (Oxford University Press 1987)

3. Equilibrium Statistical Physics, M. Plischke and B. Bergersen (World Scientific Publishing Co. Pte. Ltd., Singapore, 1994)

4. Mark Harris, Nature **456**,886-887 (2008)

5. H. Kadowaki, K. Ubukoshi, K. Hirakawa, J.L. Martinez and G. Shirane, J. Phys. Soc. Japan **56**,4027 (1987)

6. M.F. Collins and O.A. Petrenko, Can. J. Phys., **75**, 605, (1997)

7. T. Inami, M. Nishiyama, S. Maegawa and Y. Oka, Phys. Rev. B **61**, 12181 (2000)

8. A.S. Wills, A. Harrison, C. Ritter and R.I. Smith, Phys. Rev. B **61**, 6156 (2000)

9. P. Nikolic and T. Senthil, Phys. Rev. B **68** 214415 (2003)

10. T-H Han, J.S. Helton, S. Chu, D.G. Nocera, J.A. Rodriguez-Rivera, C.

Broholm and Y.S. Lee, Nature **492**, 406-410 doi:10.1038/nature11659

11. G. H. Wannier, Phys. Rev. **79**, 357 (1950)

12. Introduction to Frustrated Magnetism, edited by Claudine Lacroix, Philippe Mendels, and Frederic Mila (Springer Berlin Heidelberg, 2011)

13. A. P. Ramirez, Nature **421**, 483 (2003).

14. R. Moessner and J. T. Chalker, Phys. Rev. Lett. **80**, 2929 (1988)

15. See, for example, Frustrated Spin Systems, edited by H.T. Diep (World Scientific, Singapore, 2004)

16. C. Lacroix, P. Mendels, and F. Mila, “Introduction to frustrated magnetism” (Springer Series in Solid-State Sciences, Heidelberg, 2011)

17. L. Pauling, J. Am. Chem. Soc. **57**, 2680 (1935)

18. J.S. Gardner, G. Ehlers, S.T. Bramwell and B.D. Gaulin, J. Phys.: Condens. Matter **16** S643-S651 (2004)

19. J.E. Greedan, N.P. Raju, A. Maignan, C. Simon, J.S. Pedersen, A.M. Niraimathi, E. Gmelin, and M.A. Subramanian, Phys. Rev. B **54** 7189 (1996)

20. B.D. Gaulin, J.N. Reimers, T.E. Mason and Z. Tun, Phys. Rev. Lett. **69** 3244 (1992)

21. J.E. Greedan, J.N. Reimers, C.V. Stager, and S.L. Penny, Phys. Rev. B **43**, 5682 (1991)

22. M.J.P. Gingras, C.V. Stager, N.P. Raju, B.D. Gaulin, and J.E. Greedan, Phys. Rev. Lett. **78**, 947 (1997)

23. J.S. Gardner, S.R. Dunsiger, B.D. Gaulin, M.J.P. Gingras, J.E. Greedan, R.F. Kiefl, M.D. Lumsden, W.A. MacFarlane, N.P. Raju, J.E. Sonier, I. Swainson and Z. Tun, Phys. Rev. Lett. **82**, 1012 (1999)

24. J. S. Gardner, B. D. Gaulin, A. J. Berlinsky, and P. Waldron, Phys. Rev. B, **64**, 224416, (2001)

25. J.S. Gardner, A. Keren, G. Ehlers, C. Stock, Eva Segal, J.M. Roper, B. Fak, M.B. Stone, P.R. Hammar, D.H. Reic and B.D. Gaulin, Phys. Rev. B **68**, 180401 (2003)

26. B.C. den Hertog and M.J.P. Gingras, Phys. Rev. Lett. **84**, 3430 (2000)

27. M.J. Harris, S.T. Bramwell, D.F. McMorrow, T. Zeiske, and K.W. Godfrey, Phys. Rev. Lett. **79**, 2554 (1997)

28. S.T. Bramwell and M.J.P. Gingras, Science **294**, 1495 (2001)

29. K.A. Ross, L. Savary, B.D. Gaulin, and L. Balents, Phys. Rev. X **1**, 021002 (2011)

30. K. Kimura, S. Nakastsuji, J-J. Wen, C. Broholm, M.B. Stone, E. Nishibori

and H. Sawa, Nature Communications **4**, 1934 (2013)

31. J. Gardner, M. Gingras, J. Greedan, Reviews of Modern Physics **82**, 53 (2010)

32. M. J. Gingras, B. C. den Hertog, M. Faucher, J.S. Gardner, S. R. Dunsiger, L. J. Chang, B. D. Gaulin, N. P. Raju. and J. E. Greedan, Phys. Rev. B **62**, 6496 (2000)

33. M. T. Hutchings, "Point–charge calculation of energy levels of magnetic ions in crystalline electric fields", Solid State Phys **16**, 227 (1964)

34. K. W. H. Stevens, Proc. Phys. Soc., London, Sect. A 65, 209 (1952)

35. I. Mirebeau, P. Bonville, and M.Hennion, Phys. Rev. B **76**, 184436 (2007)

36. A Bertin, Y Chapuis, P Dalmas de Reotier and A Yaouanc, J. Phys.: Condens. Matter **24** 256003 (2012)

37. Y-J Kao, M. Enjalran, A. Del Maestro, H. R. Molavian, and M. J. P. Gingras Phys. Rev. B **68** 172407 (2003)

38. N. Hamaguchi, T. Matsushita, N. Wada, Y. Yasui, M. Sato, Phys. Rev. B **69**, 132413 (2004)

39. Y. Yasui, M. Kanada, M. Ito, H. Harashina, M. Sato, H. Okumura, K. Kakurai, H. Kadowaki, J. Phys. Soc. Japan **71,** 599 (2002)

40. E. Lhotel, C. Paulsen, P. Dalmas de Reotier, A. Yaouanc, C. Marin and S.

Vanishri, Phys. Rev. B **86**, 020410 (2012)

41. K. Fritsch, K.A. Ross, Y. Qiu, J.R.D. Copley, T. Guidi, R.I. Bewley, H.A. Dabkowska, and B.D. Gaulin, Phys. Rev. B **87**, 094410 (2013)

42. T. Fennell, M. Kenzelmann, B. Roessli, M.K. Haas and R.J. Cava, Phys. Rev. Lett. **109**, 017201 (2012)

43. T. Fennell, P.P. Deen, A.R. Wildes, K. Schnalzl, D. Prabhakaran, A.T. Boothroyd, R.J. Aldus, D.F. McMorrow, S.T. Bramwell, Science **326**, 415 (2009)

44. J. Clancy, J.P.C. Ruff, S.R. Dunsiger, Y. Zhao, H.A. Dabkowska, J.S. Gardner, Y. Qiu, J.R.D. Copley, T. Jenkins, and B.D. Gaulin, Phys. Rev. B **79**, 14408 (2009)

45. A. Ramirez, A. Hayashi, R. Cava, R. Siddardthan, B. Shastry, Nature **399**, 333 (1999)

46. Sylvain Petit, Pierre Bonville, Julien Robert, Claudia Decorse and Isabelle Mirebeau, arXiv: 1210.1428 (2012)

47. H. R. Molavian, M. J. P. Gingras, and B. Canals, Phys. Rev. Lett. **98**, 157204 (2007)

48. Kate A. Ross, Lucile Savary, Bruce D. Gaulin, and Leon Balents, Phys. Rev. X, **1**, 021002 (2011)
49. Pierre Bonville, Phys, Rev, B **84**, 184409 (2011)

50. Matsuhira K, Hinatsu Y, Tenya K, Amitsuka H and Sakakibara T 2002 J. Phys. Soc. Japan **71** 1576

51. I. Mirebeau, A. Apetrei, J. Rodriguez-Carvajal, P. Bonville, A. Forget, D. Colson, V. Glazkov, J. P. Sanchez, O. Isnard and E. Suard, Phys, Rev. Lett, **94**, 246402 (2005)

52. P. Dalmas de Reotier, A. Yaouanc, L. Keller, A. Cervellino, B. Roessli, C. Baines, A. Forget, C. Vaju, P.C.M. Gubbens, A. Amato, and P.J.C. King, Phys. Rev. Lett. **96**, 127202 (2006)

53. K.C. Rule, G. Ehlers, J.S. Gardner, Y. Qiu, E. Moskvin, K. Kiefer and S. Gerischer, J. Phys.: Condens. Matter **21** 486005 (2009)

54. F. Bert, P. Mendels, A. Olariu, N. Blanchard, G. Collin, A. Amato, C. Baines, and A. D. Hillier, Phys. Rev. Lett. **97**,117203 (2006)

Chapter 2

Neutron Scattering

2.1 Introduction to Scattering

Scattering experiments can be performed to study the structural, magnetic and dynamical properties of condensed matter. We will be primarily interested in the materials which crystallize into a crystal lattice with a regular periodic arrangement of atoms.

A scattering experiment is initiated by a beam of particles, which are typically photons, neutrons and electrons, with a certain energy. These fall incident onto a scattering system that is the material we are interested in. The incident particles interact with the atoms and usually transfer energy and momentum to the scattering system, eventually being scattered into a new direction, and with a new energy. The pattern of the intensity of the scattered particles as a function of scattered angle or/and energy can tell us a lot of information about the properties of the system under study.

Neutron scattering is a powerful tool to probe condensed matter at the microscopic levels, and is an especially important probe of the magnetic properties. The advantage of neutron scattering comes mainly from the important properties of the neutron itself. Therefore, in the next section, I will introduce the properties of the neutron. I will then talk about diffraction which is a special case of scattering in general — elastic scattering. Next, I will explain some details of neutron scattering from a theoretical view for both nuclear and magnetic scattering. At the end of this chapter, I will introduce the time-of-flight neutron scattering technique and the chopper spectrometer used in the experiments described in this thesis.

2.2 Basics Properties of the Neutron

Neutrons are produced at nuclear reactors or spallation sources. Thermal neutrons are used in our experiment. The mass, the lack of electrical charge, the energy and the magnetic moment of the thermal neutron determine its importance in scattering experiments [1].

Firstly, the mass of a neutron is 1.675×10^{-27}kg and this gives rise to the de Broglie wavelength of a thermal neutron being the order of atomic spacings in solids. Therefore, interference effects can occur and give us information about the crystal structure and other structural information of the system under study. Secondly, neutrons are neutral particles so that they can deeply penetrate into the sample. Therefore, neutrons are not scattered directly from the electron clouds in solids but rather are scattered from the nuclei in solids via the nuclear force. Thirdly, for thermal neutrons, their energy is on the order of the elementary excitations in solids, which means, the inelastic scattering, by creating or annihilating an excitation, can lead to a large change in the neutron’s energy. Thus, inelastic neutron scattering can be used to study the dynamics and excitations of condensed matter. Finally, the neutron carries a spin 1/2, with a magnetic dipole moment of $\mu_n = -1.913\mu_N$. Therefore, neutrons can interact with the unpaired electrons in a magnetic ion magnetically. Elastic magnetic scattering provides us with the microscopic magnetic structure of a magnetic material and the inelastic scattering tells us about the magnetic fluctuations and elementary excitations in the solid.

We mentioned elastic and inelastic scattering above, which are distinguish from each other by looking at whether there is energy transfer between the neutron and the sample during the scattering process. Neutron scattering is usually described by the momentum and energy transfer and these two quantities are conserved during the scattering process. If the neutron is scattered without gaining or losing energy but only with a momentum transfer to the scattering system, this process is referred to as elastic scattering or diffraction. If both the energy and momentum are transferred to the system under study, this process is called inelastic scattering. In the next section, we will briefly introduce elastic scattering.

2.3 Diffraction

As is well known, every crystal structure has two associated lattices, one is the real lattice and the other one is the reciprocal lattice. There are also two equivalent ways to describe diffraction. One of them is the Bragg formulation studied in real space while the other is the Laue formulation studied in reciprocal space [2]. Diffraction can tell us a lot of structural information about the materials in question such as the nature of ordered states and phase transitions between them. Here we introduce the two formulations of diffraction respectively.

Figure 2.1 shows the diffraction geometry which demonstrates Bragg's Law. The incident beams are reflected by the parallel atomic planes, with a spacing between them of d. Diffraction occurs when the reflected beams from parallel lattice planes interfere constructively, which means that the path difference

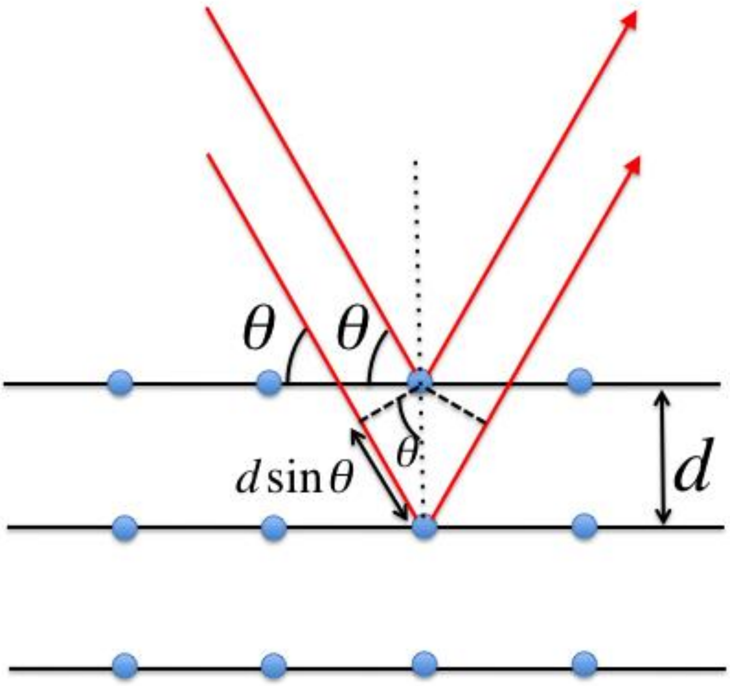

Figure 2.1: Diffraction geometry of Bragg Law: $2d\sin(\theta) = n\lambda$ [3].

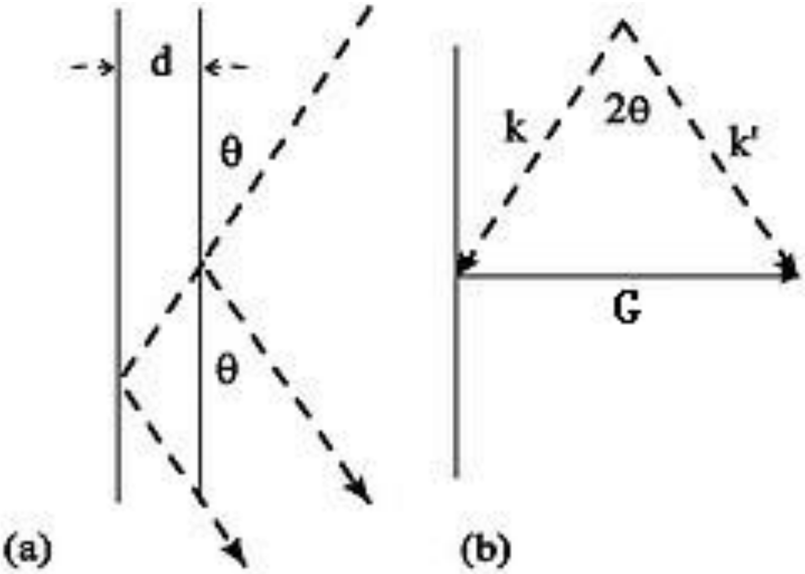

Figure 2.2: Geometries of (a) Bragg Law and (b) Laue condition

between two reflected beams from adjacent planes, $2\mathrm{d}\sin(\theta)$, is an integer, n, multiplying the wavelength λ, so

$$2\mathrm{d}\sin(\theta) = \mathrm{n}\lambda \qquad (2.1)$$

where θ is the angle of incidence. This is the well known Bragg's Law [3].

Now, let's turn to another equivalent formulation in reciprocal space to demonstrate the condition for diffraction. As shown in Fig. 2.2 (b), diffraction also occurs when the scattering vector, **Q**=**k**-**k'**, coincides with the reciprocal vector **G** of the solid, so

$$\mathbf{Q}=\mathbf{k}-\mathbf{k'}=\mathbf{G} \qquad (2.2)$$

where **k** and **k'** are initial and final wavevectors respectively. By multiplying $\hbar$ to Equation 2.2, we get

$$\hbar\mathbf{Q}= \hbar\mathbf{k}- \hbar\mathbf{k'}= \hbar\mathbf{G}$$

$$\Delta\mathbf{p}=\mathbf{p}-\mathbf{p'}= \hbar\mathbf{G} \qquad (2.3)$$

where **p** and **p'** are initial and final momenta of the beam, $\Delta\mathbf{p}$ is the momentum change. Therefore, Equation 2.3 represents momentum conservation during the scattering process.

Equation 2.1 and Equation 2.2 are equivalent and the relation between them can be demonstrated [2]. The reciprocal vector **G** is an integer, n, multiplying the shortest reciprocal vector $\mathbf{G}_0 = \frac{2\pi}{\mathrm{d}}$. From the geometry relation depicted in Fig. 2.2, Q=2ksin(θ), where k can also be written as $\frac{2\pi}{\lambda}$. Therefore, we get

$$\mathrm{n} \times \frac{2\pi}{\mathrm{d}} = 2\sin(\theta) \times \frac{2\pi}{\lambda} \qquad (2.4)$$

Equation 2.4 is just Equation 2.1, Bragg's Law.

Let's use a beautiful geometric construction known as the Ewald construction to interpret the diffraction condition [2]. As shown in Fig. 2.3, the points are reciprocal lattice points of the crystal and k is the incident wave vector. We draw a sphere centered on the tip of **k** with a radius of $\mathrm{k} = \frac{2\pi}{\lambda}$, and

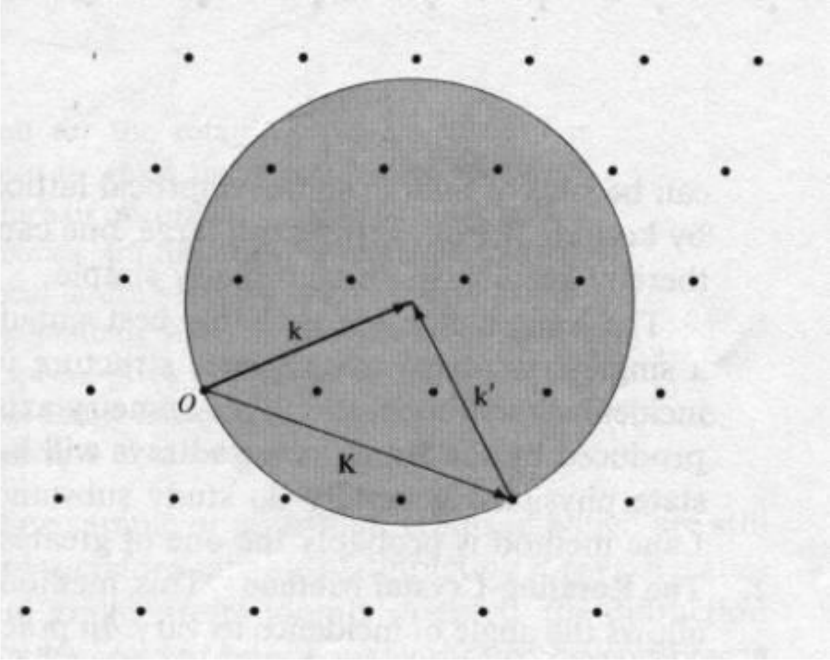

Figure 2.3: The Ewald construction [2].

we set the origin of **k** at a reciprocal lattice point. The Laue condition is satisfied only if the surface of the sphere intersects other reciprocal lattice points, so **k'** is the diffracted beam with **k'**=**k**-**G**.

2.4 Neutron Scattering

Having discussed diffraction (i.e. elastic scattering), let's now talk about general neutron scattering from a theoretical point of view. The quantity mainly measured in a neutron scattering experiment is the partial differential cross section. We will derive this quantity theoretically for both the nuclear and the magnetic scattering cases [1, 4, 5]. In order to keep the same notation with the references, the scattering vector, **Q** introduced previously, is also represented by $\boldsymbol{\kappa}$, latter in the discussion. So for the purpose of this thesis, **Q**= $\boldsymbol{\kappa}$.

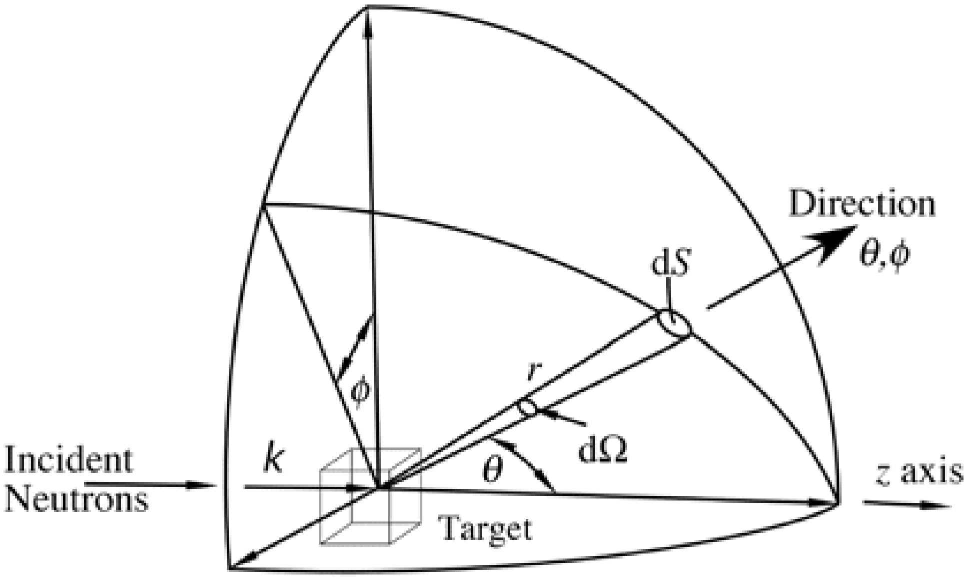

Figure 2.4: Geometry of a scattering experiment [1].

2.4.1 Nuclear Scattering

As shown is Fig. 2.4, we use polar coordinates to specify the geometry of the scattering process. Considering a monochromatic beam of incident neutrons with energy E and wavevector **k** impinging on the target which is the system under study, the neutron beam is scattered into a small solid angle $d\Omega$ in a new direction (θ, ϕ) where a detector is located to count the neutrons. By using either Bragg's law or the time of flight method, we can measure the scattered neutrons' energy, E', and wavevector, k'. We define the partial differential cross section as the fraction of neutrons scattered per second into $d\Omega$ in the direction (θ, ϕ) with a final energy between dE' and E'+dE'.

The incident neutrons with wavevector **k** can be expressed as a plane wave in the form

$$\Psi_{\mathrm{inc}} = \exp(\mathrm{ikz}). \tag{2.5}$$

And the neutrons, scattered from the point-like nuclei, have spherical, isotropic symmetry and can be written as

$$\Psi_{\mathrm{sc}} = -\frac{\mathrm{b}}{\mathrm{r}}\exp(\mathrm{ikr}) \qquad (2.6)$$

where b is the scattering length of the nuclei which can be complex. The imaginary part of b corresponds to absorption, which we are usually not considering in neutron scattering experiments. In the materials studied in this thesis, the scattering length is dominated by the real part. The value of the scattering length depends on the isotope of a given element and the spin state of the neutron-nucleus system. Only in the case of a single isotope with zero nuclear spin, the scattering is entirely coherent, otherwise the incoherent scattering presents as well.

Let's define **k** and **k'** as the initial and final states of the neutrons, and the scattering system changes states from λ to λ' during the scattering process. The number of transitions per second in $\mathrm{d}\Omega$ from **k**, λ to **k'**, λ' is given by the Fermi's golden rule,

$$\sum_{\mathbf{k}' \,\mathrm{in}\, \mathrm{d}\Omega} \mathrm{W}_{\mathbf{k},\lambda\rightarrow\mathbf{k}',\lambda'} = \frac{2\pi}{\hbar}\rho_{\mathbf{k}'}|<\mathbf{k}'\lambda'|\mathrm{V}|\mathbf{k}\,\lambda>|^2 \qquad (2.7)$$

where V is interaction potential between the neutron and the nucleus of the crystal. By considering energy conservation during the scattering process, the partial differential cross section becomes

$$\left(\frac{d^2\sigma}{d\Omega dE'}\right)_{\lambda\rightarrow\lambda'} = \left(\frac{m}{2\pi\hbar^2}\right)^2\frac{k'}{k}|<\boldsymbol{k}'\lambda'|V|\boldsymbol{k}\lambda>|^2\delta(E_\lambda - E_{\lambda'} + E - E') \qquad (2.8)$$

where E and E' are the initial and final energies of neutrons, and E_λ and $\mathrm{E}_{\lambda'}$ are the initial and final energies of the sample. The δ function is to ensure the energy change of the neutron is equal to the energy change in the system under study.

Next, by adopting the Fermi pseudopotential

$$\mathrm{V}(\mathbf{r}) = \frac{2\pi\hbar^2}{m}\mathrm{b}\delta(\mathbf{r}), \qquad (2.9)$$

and expressing the δ function of energy as a integral with respect to time

$$\delta(E_\lambda - E_{\lambda'} + E - E') = \frac{1}{2\pi\hbar}\int_{-\infty}^{\infty} \exp\left\{\frac{i(E_{\lambda'} - E_\lambda)t}{\hbar}\right\}\exp(-i\omega t)\, dt\ , \tag{2.10}$$

as well as summing over all final states λ' of the sample and averaging over all the initial states λ of the sample, we eventually get that

$$\frac{d^2\sigma}{d\Omega dE'} = \frac{k'}{k}\frac{1}{2\pi\hbar}\sum_{jj'} \overline{b_j b_{j'}} \int_{-\infty}^{\infty} < \exp\{-i\boldsymbol{\kappa}\cdot\boldsymbol{R}_{j'}(0)\}\exp\{i\boldsymbol{\kappa}\cdot\boldsymbol{R}_j(t)\} > \times \exp(-i\omega t)\, dt \tag{2.11}$$

where b_j and $b_{j'}$ are the scattering lengths of j$^{\text{th}}$ and j$'^{\text{th}}$ nuclei, $\boldsymbol{R}_{j'}(0)$ and $\boldsymbol{R}_j(t)$ are the position operators of the j$'^{\text{th}}$ nucleus at time zero and j$^{\text{th}}$ nucleus at time t. <> represents a thermal average. Equation 2.11 can be divided into two terms due to different values of $\overline{b_j b_{j'}}$ for j=j' ($\overline{b_j b_{j'}} = \overline{b^2}$) and j≠j' ($\overline{b_j b_{j'}}$=$(\bar{b})^2$) as follows:

$$\frac{d^2\sigma}{d\Omega dE'} = \left(\frac{d^2\sigma}{d\Omega dE'}\right)_{\text{coh}} + \left(\frac{d^2\sigma}{d\Omega dE'}\right)_{\text{inc}}$$

$$= \frac{\sigma_{\text{coh}}}{4\pi}\frac{k'}{k}\frac{1}{2\pi\hbar}\sum_{jj'}\int_{-\infty}^{\infty} < \exp\{-i\boldsymbol{\kappa}\cdot\boldsymbol{R}_{j'}(0)\}\exp\{i\boldsymbol{\kappa}\cdot\boldsymbol{R}_j(t)\} >\times \exp(-i\omega t)\, dt$$

$$+ \frac{\sigma_{\text{inc}}}{4\pi}\frac{k'}{k}\frac{1}{2\pi\hbar}\sum_{j}\int_{-\infty}^{\infty} < \exp\{-i\boldsymbol{\kappa}\cdot\boldsymbol{R}_{j}(0)\}\exp\{i\boldsymbol{\kappa}\cdot\boldsymbol{R}_j(t)\} >\times \exp(-i\omega t)\, dt \tag{2.12}$$

where $$\sigma_{\text{coh}} = 4\pi(\bar{b})^2,\ \ \sigma_{\text{inc}} = 4\pi\{\overline{b^2} - (\bar{b})^2\}. \tag{2.13}$$

The first term corresponds to coherent scattering and the second term corresponds to incoherent scattering. Coherent scattering arises from an interference effect, and the scattering is as if all the scattering lengths of the system were equal to $\bar{b}$. While incoherent scattering does not give an interference effect, it does arise from a random distribution or fluctuations of the scattering lengths from their mean value $\bar{b}$ in the system. The incoherent scattering can only provide information about individual nuclei in motion, and the correlation of the same nuclei at different times. In contrast, the coherent scattering can give us information about the correlation among different nuclei at different times.

The thermal average in the above, Equation 2.12, can also be expressed in terms of correlation functions. Let's define a function I($\boldsymbol{\kappa}$, t) known as intermediate function:

$$\mathrm{I}(\boldsymbol{\kappa},\mathrm{t}) = \frac{1}{\mathrm{N}}\sum_{jj'} < \exp\{-i\boldsymbol{\kappa}\cdot\boldsymbol{R}_{j'}(0)\}\exp\{i\boldsymbol{\kappa}\cdot\boldsymbol{R}_j(t)\} > \qquad (2.14)$$

Next, we can define the time-dependent pair-correlation function G($\mathbf{r}$, t) by momentum Fourier transform of I($\boldsymbol{\kappa}$, t)

$$\mathrm{G}(\mathbf{r},\mathrm{t}) = \frac{1}{(2\pi)^3}\int \mathrm{I}(\boldsymbol{\kappa},\mathrm{t})\exp(-\mathrm{i}\boldsymbol{\kappa}\cdot\boldsymbol{r})\,\mathrm{d}\boldsymbol{\kappa}$$

$$= \frac{1}{\mathrm{N}}\sum_{jj'}\int < \delta\{\mathbf{r}'-\boldsymbol{R}_{j'}(0)\}\delta\{\mathbf{r}'+\mathbf{r}-\boldsymbol{R}_j(t)\} > \mathrm{d}\mathbf{r}' \qquad (2.15)$$

This function tells us the probability that, given the position of a particle at time zero, any particle being a certain distance r apart at time t. The scattering function S($\boldsymbol{\kappa}, \omega$) can also be related to these two functions by

$$\mathrm{S}(\boldsymbol{\kappa},\omega) = \frac{1}{2\pi\hbar}\int \mathrm{I}(\boldsymbol{\kappa},\mathrm{t})\exp(-\mathrm{i}\omega t)\,\mathrm{d}t \qquad (2.16)$$

$$\mathrm{S}(\boldsymbol{\kappa},\omega) = \frac{1}{2\pi\hbar}\int \mathrm{G}(\mathbf{r},\mathrm{t})\exp\{\mathrm{i}(\boldsymbol{\kappa}\cdot\boldsymbol{r}-\omega t)\}\,\mathrm{d}\mathbf{r}\mathrm{d}t \qquad (2.17)$$

Therefore, the scattering function is proportional to the space and time Fourier transform of the time-dependent pair-correlation function.

S($\boldsymbol{\kappa}, \omega$) can be divided into coherent and incoherent parts, so the relationship between the scattering function and the partial differential cross section (Equation 2.12) can be written as

$$\frac{d^2\sigma}{d\Omega dE'} = \left(\frac{d^2\sigma}{d\Omega dE'}\right)_{\mathrm{coh}} + \left(\frac{d^2\sigma}{d\Omega dE'}\right)_{\mathrm{inc}}$$

$$= \frac{\sigma_{\mathrm{coh}}}{4\pi}\frac{k'}{k}N\mathrm{S}(\boldsymbol{\kappa},\omega) + \frac{\sigma_{\mathrm{inc}}}{4\pi}\frac{k'}{k}N\mathrm{S}_{\mathrm{i}}(\boldsymbol{\kappa},\omega) \qquad (2.18)$$

2.4.2 Magnetic Scattering

Since neutrons have a magnetic moment given by

$$\boldsymbol{\mu}_{\mathrm{n}} = -\gamma\mu_{\mathrm{N}}\boldsymbol{\sigma} = -\gamma\frac{\mathrm{e}\hbar}{2\mathrm{m_p}}\boldsymbol{\sigma} \qquad (2.19)$$

Therefore, if the system contains magnetic ions, the magnetic interaction between the neutron spin and the magnetic field generated by the unpaired electrons of the magnetic ions is given by the Zeeman interaction [6]

$$\mathrm{V_m} = \boldsymbol{\mu}_\mathrm{n} \cdot \mathbf{B} \tag{2.20}$$

where **B** arises from two terms: the spin ($\mathbf{B}_\mathrm{S}$) and orbital motion ($\mathbf{B}_\mathrm{L}$) of an electron. The magnetic potential becomes

$$\mathrm{V_m} = -\frac{\mu_0}{4\pi}\gamma\mu_\mathrm{N} 2\mu_\mathrm{B} \boldsymbol{\sigma} \cdot \left(\mathrm{curl}\left(\frac{\mathbf{s}\times\widehat{\mathbf{R}}}{\mathrm{R}^2}\right) + \frac{1}{\hbar}\frac{\mathbf{p}\times\widehat{\mathbf{R}}}{\mathrm{R}^2}\right) \tag{2.21}$$

where **s** and **p** represent the spin and momentum operators of an electron. $\widehat{\mathbf{R}}$ is the unit vector of **R**, the position vector of the magnetic field from the electron. Substituting $\mathrm{V_m}$ into the general expression for the partial differential cross section

$$\left(\frac{d^2\sigma}{d\Omega dE'}\right)_{\sigma\lambda\to\sigma'\lambda'} = \left(\frac{m}{2\pi\hbar^2}\right)^2 \frac{k'}{k} |< \sigma'\boldsymbol{k}'\lambda'|\mathrm{V}|\sigma\boldsymbol{k}\lambda >|^2 \delta(E_\lambda - E_{\lambda'} + \hbar\omega) \tag{2.22}$$

in which we specify the initial and final spin states of the neutron as (σ, σ‘) respectively, we arrive at the result

$$\left(\frac{d^2\sigma}{d\Omega dE'}\right)_{\sigma\lambda\to\sigma'\lambda'} = (\gamma r_0)^2 \frac{k'}{k} |< \sigma'\lambda'|\boldsymbol{\sigma}\cdot\mathbf{Q}_\perp|\sigma\lambda >|^2 \delta(E_\lambda - E_{\lambda'} + \hbar\omega) \tag{2.23}$$

where $$\mathbf{Q}_\perp = \sum_\mathrm{i} \exp(\mathrm{i}\boldsymbol{\kappa}\cdot\boldsymbol{r_i})\left\{\widehat{\boldsymbol{\kappa}} \times (\mathbf{s}_\mathrm{i} \times \widehat{\boldsymbol{\kappa}}) + \frac{\mathrm{i}}{\hbar\kappa}(\mathbf{p}_\mathrm{i} \times \widehat{\boldsymbol{\kappa}})\right\} \tag{2.24}$$

is related to the magnetization of the scattering system. The perpendicular symbol means that magnetic scattering is only sensitive to the component of the magnetic moments perpendicular to the scattering vector. By summing over the final states (σ', λ') and averaging over the initial states (σ, λ), we get a more useful expression for partial differential cross section,

$$\frac{d^2\sigma}{d\Omega dE'} = (\gamma r_0)^2 \frac{k'}{k} \sum_{\alpha\beta}(\delta_{\alpha\beta} - \hat{\kappa}_\alpha\hat{\kappa}_\beta) \sum_{\lambda\lambda'} p_\lambda < \lambda|Q_\alpha^+|\lambda' >< \lambda'|Q_\beta|\lambda > \\ \times \delta(E_\lambda - E_{\lambda'} + \hbar\omega) \tag{2.25}$$

where $\sum_{\alpha\beta}(\delta_{\alpha\beta} - \hat{\kappa}_\alpha\hat{\kappa}_\beta)$ again confirms that only the component of magnetic moments perpendicular to the scattering vector contributes to the magnetic scattering. This equation is the basic equation used in the theoretical calculation in Chapter 3.

Again, by using the property that the delta function can be expressed in terms of the integral with respect to time, we can obtain the partial differential cross section in terms of the spin correlation function,

$$\frac{d^2\sigma}{d\Omega dE'} = \frac{(\gamma r_0)^2}{2\pi\hbar}\frac{k'}{k} N \left\{\frac{1}{2} gF(\boldsymbol{\kappa})\right\}^2 \sum_{\alpha\beta}(\delta_{\alpha\beta} - \hat{\kappa}_\alpha\hat{\kappa}_\beta) \sum_l \exp(i\boldsymbol{\kappa}\cdot\boldsymbol{l}) \times$$
$$\int_{-\infty}^{\infty} < \exp\{-i\boldsymbol{\kappa}\cdot\boldsymbol{u}_0(0)\} \exp\{i\boldsymbol{\kappa}\cdot\boldsymbol{u}_l(t)\} > < S_0^\alpha(0) S_l^\beta(t) > \exp(-\mathrm{i}\omega t)\,\mathrm{d}t \tag{2.26}$$

Considering the partial differential cross section for nuclear scattering in Equation 2.8 and magnetic scattering in Equation 2.25, the intensity would specify a set of delta functions which ensure energy conservation during the scattering process. However, these infinite sharp peaks are replaced by the peaks with finite widths in real experiments. This is mainly due to reasons such as the mosaic spread of the crystal, the resolution of the instrument and the specific properties of the scattering system. Therefore, we usually use the convolution of the resolution function $\mathrm{R}(\boldsymbol{\kappa} - \boldsymbol{\kappa}_0, \omega - \omega_0)$ and the scattering function $\mathrm{S}(\boldsymbol{\kappa}, \omega)$ to describe the signal measured in a neutron scattering experiment as follows

$$\mathrm{I}(\boldsymbol{\kappa}_0, \omega_0) = \int \mathrm{S}(\boldsymbol{\kappa}_0, \omega_0)\mathrm{R}(\boldsymbol{\kappa} - \boldsymbol{\kappa}_0, \omega - \omega_0)\mathrm{d}\,\boldsymbol{\kappa} d\omega \tag{2.27}$$

The resolution function is peaked at $(\boldsymbol{\kappa}_0, \omega_0)$ and falls off when deviating from $(\boldsymbol{\kappa}_0, \omega_0)$.

2.5 Instrumentation

The neutron scattering measurements in Chapters 3 and 4 were performed on the SEQUOIA direct geometry time-of-flight spectrometer at the Spallation Neutron Source (SNS) of Oak Ridge National Laboratory. Therefore, we will only consider this technique and instrument in this section.

2.5.1 The Time-of-Flight Technique

The triple axis technique is a well known neutron scattering technique. However, in this original manifestation, it had a limitation that only one specific point in (**Q**,w) phase space can be measured at a time. The time-of-flight technique is a good complement to the triple axis method. The neutron interacts with the sample, gaining or losing energy, and then is scattered with a new velocity. Therefore, the arrival time of the neutron from the sample to the detectors varies. A series of detectors around the sample can be arranged and they can cover a large scattering angle so that they can collect the scattered neutrons with several wavevectors and energies at the same time. Therefore, time-of-flight technique can measure a large region of (**Q**,w) phase space simultaneously.

SNS is one of the neutron facilities at Oak Ridge National Laboratory. It is formed by a linear proton accelerator followed by a ring-shaped accumulator facility, which can produce high energy protons, periodically ejected from the accumulator ring as a pulse. These pulses of protons strike onto a heavy metal target, Hg, where the spallation occurs. The spallation neutrons occur in pulses moderated by the room temperature water moderator at the beam line. These thermal neutrons are guided through the beam line to our SEQUIA spectrometer shown in Figure 2.5.

SEQUOIA is a fine resolution, Fermi chopper time-of-flight spectrometer utilizing the incident neutron energies E_i between 10meV to 2eV [7, 8]. Neutrons are guided through the neutron guide to ensure a high flux of the incident beam on the sample. A T_0 chopper located 9.861m from the moderator is used to block the fast neutrons generated when the proton pulse hits the target. It works by scattering fast neutrons into the neighbor shielding, while then being out of beam to allow the desirable 10 meV~2 eV neutron to pass. Then, a Fermi chopper located 18.0085 m from the moderator

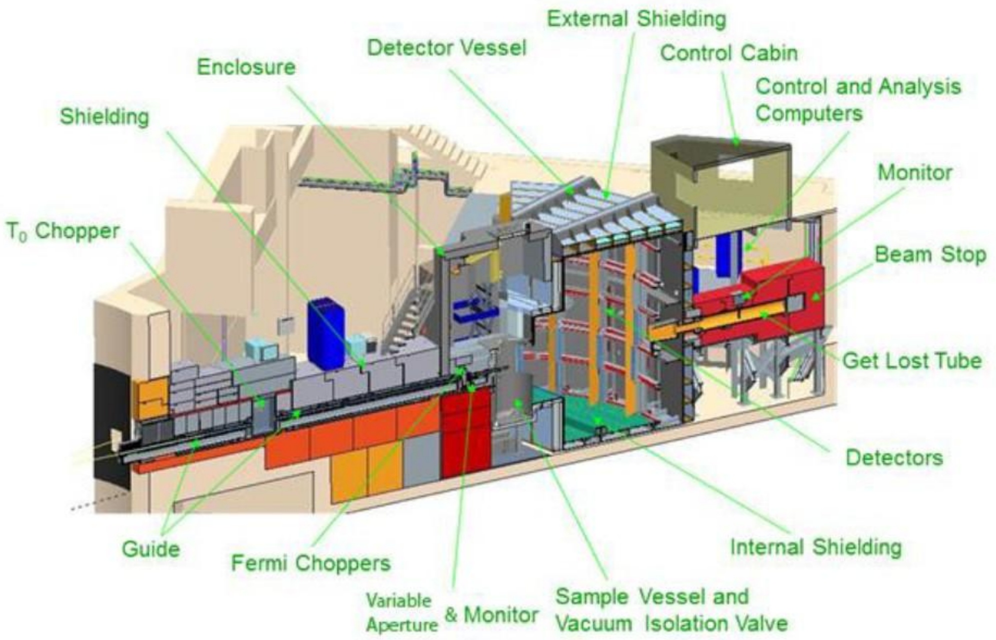

Figure 2.5: Schematic of the SEQUOIA. [7]

monochromates the neutron beam. The Fermi chopper consists of a series of closely spaced neutron-absorbing blades within slits, spinning about a vertical axis of the beam path at some frequency. Combined with the frequency of T_0 chopper, only the neutrons with a desired velocity, or energy window, can pass through the slits of the Fermi chopper and reach the sample. The sample is located 20 m from the moderator. After interacting with the sample, neutrons are scattered to the detectors located 5.5 m downstream from the sample position. A cylindrical array of 1440 detectors, each 1.2 m long by 25 mm wide, covers a scattering angle plane from -30° to 60° in the horizontal and ±18° in the vertical.

From the name time-of-flight, we know that the main measurement in this technique is time. The initial and final energies of neutrons can be measured by the time (t_1) the neutrons take to travel from the Fermi chopper to sample position and the time (t_2) the neutrons take to travel from the sample position to the detector. Given the initial energy (E_0) or velocity (v_0) of neutrons, the distance (L_0) between the Fermi chopper to the sample position and the distance (L_1) between the sample position to the detector, the final energies (E_f) or velocities (v_f) of scattered neutrons can be obtained by measuring the total time traveling from the Fermi chopper:

$$t = t_0 + t_1 = \frac{L_0}{v_0} + \frac{L_1}{v_f} \qquad (2.28)$$

Once v_f is determined, the final energy (E_f) and the energy transfer ($E_0 - E_f$) is determined as well. Meanwhile, by measuring the direction of the scattered neutron, the wavevector transfer (**Q**=**k**-**k’**) is also determined. Therefore, one can measure the energy transfer and the wavevector transfer simultaneously over a large range of reciprocal space.

Bibliography

1. Introduction to the theory of thermal neutron scattering, G.L. Squires (Cambridge University Press, Orlando, 1987)

2. Solid State Physics, N.W. Ashcroft and N.D. Mermin (Nelson Thompson Learning, Toronto, 1976)

3. Introduction to Solid State Physics, Charles Kittel (University of California, Berkeley, 2005)

4. Neutron Scattering with a Triple-Axis Spectrometer, G. Shirane, S.M. Shapiro, and J.M. Tranquada (Cambridge University Press, 2002)

5. Magnetic Critical Scattering, M.F. Collins (Oxford University Press, New York, 1989)

6. X-ray and Neutron Reflectivity: Principles and Applications, J. Daillant and A. Gibaud (Springer, Berlin Heidelberg 2009)

7. SEQUOIA Operations Manual for Users, G.E. Granroth, A.I. Kolesnikov, T.E. Sherline, 2012

8. G.E. Granroth, A.I. Kolesnikov, T.E. Sherline, J.P. Clancy, K.A. Ross, J.P.C. Ruff, B.D. Gaulin, S.E. Nagler, Journal of Physics: Conference of Series **251**, 012058 (2010)

Chapter 3

Neutron Spectroscopic Study of Crystal Field Excitations in $\mathbf{Tb_2Ti_2O_7}$ and $\mathbf{Tb_2Sn_2O_7}$

3.1 Introduction

The contents of this chapter are based on a manuscript which is in preparation for publication. Here, I would like to mention and acknowledge many people's help in the work of this chapter. First, I wish to thank Prof. Cava's group in the Department of Chemistry at Princeton University for the synthesis of the samples. Second, I wish to thank Katharina Fritsch and Bruce Gaulin for their help while we were doing the neutron scattering measurements in Oak Ridge National Lab in May, 2012. Third, I also want to thank Michel Gingras's students for helping me learn the related theoretical calculations. Finally, I would like to thank my supervisor, Bruce Gaulin, as he and I co-wrote this chapter, as a manuscript which will be submitted for publication.

The purpose of this study is to probe the crystal field excitations in $\mathrm{Tb_2Ti_2O_7}$ and $\mathrm{Tb_2Sn_2O_7}$ experimentally and to understand them theoretically. Different research groups have performed such work to probe the crystal field eigenvalues and eigenfunctions using inelastic neutron scattering for many different $\mathrm{R_2M_2O_7}$ pyrochlores over an extended period of time

[1-7]. The crystal field states are associated with the total angular momentum **J**, that results from applying Hund's rules to the appropriate number of 4f electrons associated with the R^{3+} site. These determine the size and anisotropy of the R^{3+} magnetic moment in its ground state. All the information of the size, anisotropy, and ultimately the wavefunction associated with the ground state magnetic moment is an essential starting point to the full description of their exotic low temperature properties in the $R_2M_2O_7$ pyrochlores. However, the crystal field eigenvalues in these systems can extend to energies of ~100 meV, and the unique determination of the eigenvalues and eigenfunctions of these crystal field levels is not necessarily straightforward.

Specifically, one important case is the crystal field eigenfunctions and eigenvalues for Tb^{3+} in $Tb_2Ti_2O_7$ and $Tb_2Sn_2O_7$. For both materials, the low lying crystal field excitations have been previously studied using triple axis neutron scattering techniques [1,7]. The picture of a ground state doublet separated by ~1.5 meV from an excited state doublet in both materials has been known for some time [1,7,8]. The next highest energy eigenstates begin at ~10 meV [1,7,8]. However, the higher energy crystal field transitions were difficult to observe in previous experiments, so the nature of the crystal field eigenstates at energies large compared to ~10 meV, where at least half of the (2J+1)=13 crystal field states reside, are less well understood. Recent advances in time-of-flight neutron spectroscopy have greatly advanced our capability to measure such crystal field and other magnetic excitations over a broad dynamic range in energy. What's more, the precise details of even the low lying crystal field states which determine the ground state and low temperatures properties are overall better understood in the context of a more comprehensive study extending over a broader dynamic range in energy, as allowed by time-of-flight neutron techniques.

Therefore, it is timely to re-examine some of the earlier crystal field studies, especially in cases where the precise details of the crystal field eigenfunctions are believed to be very important to ground state selection and to the nature of the experimentally observed exotic ground state. In this chapter, we will focus on $Tb_2Ti_2O_7$ and $Tb_2Sn_2O_7$.

For the experimental work, we present new time-of-flight inelastic neutron scattering measurements on polycrystalline samples of $Tb_2Ti_2O_7$ and $Tb_2Sn_2O_7$ at energy transfers less than ~80 meV by using three different incident neutron enegies E_i, of 11 meV, 45 meV and 120 meV to probe different crystal field excitations. These measurements are performed at two temperatures, 1.5 K and 30 K, such that we can observe transitions both out of the ground state doublet alone, and out of both the ground state and first excited state doublet. At both at T=1.5 K or at T=30 K, quite different crystal field excitations can be observed in $Tb_2Ti_2O_7$ and $Tb_2Sn_2O_7$. For the theoretical work, parameters describing the crystal fields appropriate to both $Tb_2Ti_2O_7$ and $Tb_2Sn_2O_7$ are determined by fitting these measurements to the results of crystal field calculations and magnetic neutron scattering cross section calculations. The eigenfunctions and eigenvalues appropriate to both $Tb_2Ti_2O_7$ and $Tb_2Sn_2O_7$ are then determined. The overall scale for the crystal field splitting of the (2J+1)=13 crystal field levels is almost a factor of 2 greater in $Tb_2Ti_2O_7$ compared with $Tb_2Sn_2O_7$. Our results are consistent with previous measurements on crystal field states in $Tb_2Sn_2O_7$, wherein the ground state doublet corresponds primarily to $J_z = |\mp 5>$, and the first excited state doublet to $J_z = |\mp 4>$. In contrast, our results on $Tb_2Ti_2O_7$ differ from earlier studies and show the ground state doublet to correspond to a significant mixture of $J_z = |\mp 5>, J_z = |\pm 4> \mathit{and}\, J_z = |\mp 2>$, while the first excited state doublet corresponds to a mixture of $J_z = |\pm 4>, J_z = |\mp 5> \mathit{and}\, J_z = |\pm 1>$.

The experimental details are as follows.

Powder samples of $\mathrm{Tb_2Ti_2O_7}$ and $\mathrm{Tb_2Sn_2O_7}$ were synthesized by mixing high purity $\mathrm{Tb_4O_7}$ with $\mathrm{TiO_2}$ and $\mathrm{SnO_2}$, respectively in the appropriate stoichiometric ratios, and placing these in high density aluminum oxide crucibles. The materials were fired in air for two days, with intermediate grinding, at temperatures of 1100, 1200, 1300 and finally 1350 ℃. Powder X-ray diffraction measurements showed high quality single phase materials displaying the cubic space group of $\mathrm{Fd\bar{3}m}$.

Inelastic neutron scattering measurements were performed on the SEQUOIA direct geometry time-of-flight spectrometer at the Spallation Neutron Source of Oak Ridge National Laboratory. Two samples were measured: $\mathrm{Tb_2Ti_2O_7}$ and $\mathrm{Tb_2Sn_2O_7}$. Measurements were performed at T=1.5 K and T=30 K, and over a wide dynamic range of energies, using incident neutron energies, $\mathrm{E_i}$, of 11 meV, 45 meV and 120 meV, in order to probe the crystal field excitations over a large range in energy. Measurements employing higher incident energies cover a larger dynamic range in energy, and correspond to coarser energy resolution, which typically corresponds to 2-3% of $\mathrm{E_i}$.

Two 100 mm in diameter Fermi choppers were used for these measurements: the coarse resolution chopper had a 3.5 mm slit spacing and the fine resolution chopper had a 2 mm slit spacing. For $\mathrm{E_i}$= 120 meV, the coarse resolution chopper was spun at 300 Hz and the T0 chopper was spun at 180 Hz. The fine resolution chopper was spun at 180 Hz and 420 Hz for $\mathrm{E_i}$ =11 meV and 45 meV, respectively. For $\mathrm{E_i}$=11 meV, the T0 chopper operated at 60 Hz and for $\mathrm{E_i}$=45 meV, it operated at 90 Hz.

The powder samples of $\mathrm{Tb_2Ti_2O_7}$ and $\mathrm{Tb_2Sn_2O_7}$ were placed in a flat plate Al cell to completely cover the 5cmx5cm neutron beam, and the Al cell was mounted in an Orange ILL cryostat with a base temperarure of 1.5 K.

Background data from an empty aluminum can was subtracted from the signal. Every measurement was carried out for two hours of counting time.

3.2 Crystal Field Calculation and Magnetic Neutron Scattering Calculation

Before showing the experimental and theoretical results, I would like to review the calculations involved in this study. Actually, these calculations have already been discussed in Chapter 1 and Chapter 2. To begin, the calculation of the crystal field Hamiltonian using Equation 1.2,

$$H_{cf} = \alpha_J D_2^0 O_2^0 + \beta_J (D_4^0 O_4^0 + D_4^3 O_4^3) + \gamma_J (D_6^0 D_6^0 + D_6^3 O_6^3 + D_6^6 O_6^6) \quad (3.1)$$

where the coefficients are α_J=-1/99, β_J=2/16335, γ_J=-1/891891 for Tb^{3+}, O_n^m are Stevens operators which are functions of total angular momentum (J, J_z, J_+ and J_-). D_n^m are crystal field parameters that we are going to determine for $Tb_2Ti_2O_7$ and $Tb_2Sn_2O_7$ in this chapter. By applying the operators on the basis of |J, J_z>, only |J, J_z> will appear for O_n^0 (i.e. only diagonal matrix elements appear), and only |J, $J_z \pm 3$> and |J, $J_z \pm 6$> will appear for O_n^3 and O_6^6 respectively. These properties enable the crystal field Hamiltonian to have a matrix of the form:

$$H_{cf} = \begin{bmatrix} H_{1,1} & 0 & 0 & H_{1,4} & 0 & 0 & H_{1,7} & 0 & 0 & 0 & 0 & 0 & 0 \\ 0 & H_{2,2} & 0 & 0 & H_{2,5} & 0 & 0 & H_{2,8} & 0 & 0 & 0 & 0 & 0 \\ 0 & 0 & H_{3,3} & 0 & 0 & H_{3,6} & 0 & 0 & H_{3,9} & 0 & 0 & 0 & 0 \\ H_{4,1} & 0 & 0 & H_{4,4} & 0 & 0 & H_{4,7} & 0 & 0 & H_{4,10} & 0 & 0 & 0 \\ 0 & H_{5,2} & 0 & 0 & H_{5,5} & 0 & 0 & H_{5,8} & 0 & 0 & H_{5,11} & 0 & 0 \\ 0 & 0 & H_{6,3} & 0 & 0 & H_{6,6} & 0 & 0 & H_{6,9} & 0 & 0 & H_{6,12} & 0 \\ H_{7,1} & 0 & 0 & H_{7,4} & 0 & 0 & H_{7,7} & 0 & 0 & H_{7,10} & 0 & 0 & H_{7,13} \\ 0 & H_{8,2} & 0 & 0 & H_{8,5} & 0 & 0 & H_{8,8} & 0 & 0 & H_{8,11} & 0 & 0 \\ 0 & 0 & H_{9,3} & 0 & 0 & H_{9,6} & 0 & 0 & H_{9,9} & 0 & 0 & H_{9,12} & 0 \\ 0 & 0 & 0 & H_{10,4} & 0 & 0 & H_{10,7} & 0 & 0 & H_{10,10} & 0 & 0 & H_{10,13} \\ 0 & 0 & 0 & 0 & H_{11,5} & 0 & 0 & H_{11,8} & 0 & 0 & H_{11,11} & 0 & 0 \\ 0 & 0 & 0 & 0 & 0 & H_{12,6} & 0 & 0 & H_{12,9} & 0 & 0 & H_{12,12} & 0 \\ 0 & 0 & 0 & 0 & 0 & 0 & H_{13,7} & 0 & 0 & H_{13,10} & 0 & 0 & H_{13,13} \end{bmatrix}$$

(3.2)

By diagonalizing the crystal field Hamiltonian $\mathrm{H_{cf}}$, the crystal field eigenvalues and eigenfunctions can be determined. We can get 13 eigenvalues corresponding to 13 crystal field energy levels, and each of these eigenvalues is associated with a eigenfunction which is in terms of all the 13 local | J, $\mathrm{J_z}$> basis from $\mathrm{J_z} = -6$ to $\mathrm{J_z} = +6$.

Given a certain set of 6 crystal field parameters $\mathrm{D_n^m}$, we can calculate all the eigenvalues and eigenfunctions. So, our purpose is to determine these six parameters by comparison between the inelastic neutron scattering data and neutron scattering cross section calculation. For this reason, we should turn to the calculation of the magnetic neutron scattering cross section relevant to such crystal field states.

The magnetic neutron scattering cross section is introduced in Equation 2.25,

$$\frac{d^2\sigma}{d\Omega dE'} = (\gamma r_0)^2 \frac{k'}{k} \sum_{\alpha\beta}(\delta_{\alpha\beta} - \hat{\kappa}_\alpha \hat{\kappa}_\beta) \sum_{\lambda\lambda'} p_\lambda < \lambda|Q_\alpha^+|\lambda' >< \lambda'|Q_\beta|\lambda > \times \delta(E_\lambda - E_{\lambda'} + \hbar\omega) \qquad (3.3)$$

α and β are directions of x, y and z. $\sum_{\alpha\beta}(\delta_{\alpha\beta} - \hat{\kappa}_\alpha \hat{\kappa}_\beta)$ are the sum of all the matrix elements in the 3×3 matrix. Only diagonal terms exist (i.e. α=β=x, α=β=y, and α=β=z) in the calculation. Therefore, Equation 3.3 can be simplified to

$$\frac{d^2\sigma}{d\Omega dE'} = C \frac{k'}{k} \sum_\alpha \sum_{\lambda\lambda'} p_\lambda < \lambda|J_\alpha^+|\lambda' >< \lambda'|J_\alpha|\lambda > L_{\lambda\lambda'} \qquad (3.4)$$

where C is a constant, k and k' are the moduli of the incident and outcoming wavevectors. $\sum_\alpha \sum_{\lambda\lambda'} p_\lambda < \lambda|J_\alpha^+|\lambda' >< \lambda'|J_\alpha|\lambda >$ is the sum over the intensities of the transitions from crystal field state | λ> of energy E_λ to the crystal field state | λ'> of energy $E_{\lambda'}$, p_λ is the probability that the sample is initially in the state λ determined by the Maxwell–Boltzmann distribution, and J_α is the x, y or z component of the total angular momentum operator.

$L_{\lambda\lambda'}$ is a Lorentzian function of the excitation from state $|\lambda>$ of energy E_λ to the state $|\lambda'>$ of energy $E_{\lambda'}$:

$$L_{\lambda\lambda'} = \frac{1}{\pi}\frac{\Gamma_{\lambda\lambda'}}{{\Gamma_{\lambda\lambda'}}^2+\left(\hbar\omega-(E_{\lambda'}-E_\lambda)\right)^2} \tag{3.5}$$

This function replaces the delta function in the energy difference between the two states in Equation (3.3). As crystal field states typically have little dispersion and long lifetimes, the energy width of $L_{\lambda\lambda'}$, $\Gamma_{\lambda\lambda'}$, is usually determined by the finite instrumental energy resolution of the spectrometer. As a rule, the lower the incident energy, the better the resolution, which means the narrower the relevant inelastic peak in the spectrum.

In Equations 3.4 and 3.5, E_λ and $E_{\lambda'}$ are the eigenvalues we get in Equation 3.1 or 3.2, and $|\lambda>$ and $|\lambda'>$ are the eigenfunctions we get in Equation 3.1or 3.2. However, J_α is the component of the total angular momentum operator in the global frame. Therefore, we have to consider the transformation relation between the global axis of frame and the local axis of frame for the four Tb^{3+} in an arbitrary tetrahedron (Equation 1.3). In the eventual calculation, the cross section is the sum of four contributions from the four Tb^{3+} sites in a tetrahedron. The combination of Equation 3.1 and Equation 3.4 as well as the transformation relation in Equation 1.3 can help us reconstruct the inelastic neutron scattering spectra for comparison.

3.3 Inelastic Neutron Scattering Results and Calculation Results

In Figure 3.1, we show the T=1.5 K inelastic neutron scattering data for $Tb_2Ti_2O_7$ (left side) and $Tb_2Sn_2O_7$ (right side) taken on the SEQUOIA time-of-flight chopper spectrometer at the SNS. Figure 3.1 a), b) and c) show data for $Tb_2Ti_2O_7$ using a) E_i=11 meV, b) E_i=45 meV, and c) E_i=120 meV, while Figure 3.1 d), e) and f) show the same E_i=11, 45, and 120 meV data sets, respectively, for $Tb_2Sn_2O_7$. As nearly identical amounts of the two $Tb_2Ti_2O_7$ and $Tb_2Sn_2O_7$ powder samples were loaded into identical sample cans in the same cryostat, a direct comparison can be made between the two sets of data. These color contour maps show the full energy vs |Q| data sets. Inspection of Figure 3.1 shows a large number of excitations which are mostly identified as magnetic crystal field excitations, due to their relative lack of dispersion and their |Q| independence. The top data sets, in Figure 3.1 a) for $Tb_2Ti_2O_7$ and Figure 3.1 d) for $Tb_2Sn_2O_7$, show the relatively low energy crystal field excitations below ~8 meV, and show great similarity between the two pyrochlores. The lowest lying crystal field excitations, between 1meV and 2meV in energy, do exhibit weak dispersion in these T=1.5 K data sets in both materials, displaying a minimum around |Q|~1.25 $Å^{-1}$, as was previously known [1,9,10]. This dispersion disappears at temperatures large compared to θ_{CW}, and it is not observed in our T=30 K data sets which will be shown later in Figure 3.2. This low temperature dispersion is consistent with the short range order at low temperatures. Clear differences between $Tb_2Ti_2O_7$and $Tb_2Sn_2O_7$ are evident at intermediate energies, up to ~40 meV as seen in Figure 3.1 b) and e), and these differences persist to the highest energies measured, ~90 meV, as shown in Figure 3.1 c) and f).

Consistent with previous measurements, we see that the lowest energy crystal field excited states, at the minimum of their dispersion, in either $Tb_2Ti_2O_7$ or $Tb_2Sn_2O_7$ is at ~1 meV ~11 K, and therefore the base temperature of T=1.5 K assures us that we are observing transitions out of the ground state only. As the lowest lying excited crystal field states are confined to energies less than 2 meV ~22 K, and the next highest energy crystal field states are at ~10 meV ~110 K, our measurements at T=30 K in Figure 3.2 will correspond to the ground state and first excited state crystal field excitations

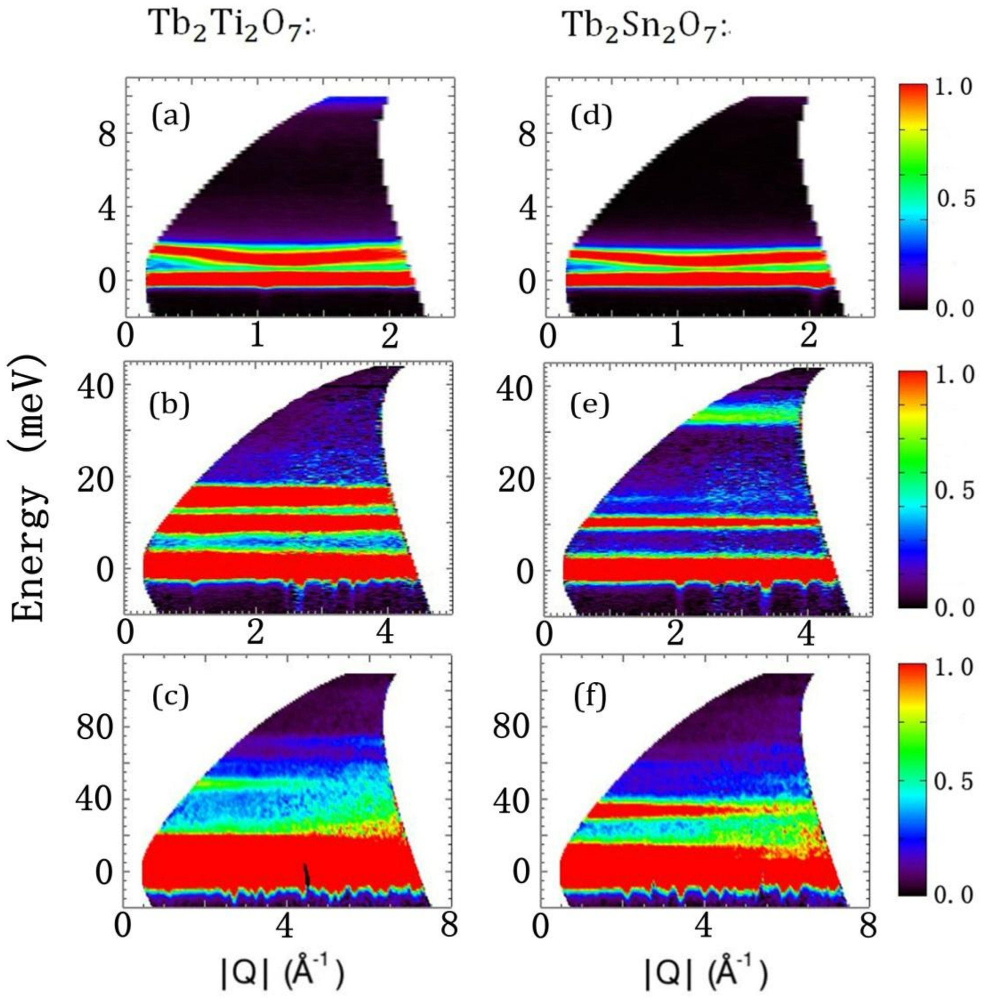

Figure 3.1: Color contour maps of energy vs |Q| from the inelastic neutron scattering data for $Tb_2Ti_2O_7$ and $Tb_2Sn_2O_7$ at T=1.5 K are shown. The top two plots show data at relatively low energies taken with E_i=11 meV neutrons. Well defined transitions between the ground state crystal field doublet and the lowest excited state crystal field doublet between 1-2 meV as well as weak dispersion of this excitation, are observed for both samples. The middle panel shows data up to ~43 meV, using E_i=45 meV neutrons. The bottom two plots show data taken to the highest energy transfers, using E_i=120 meV neutrons. All data sets shown are for T=1.5 K. An empty can background was subtracted and the data were corrected for detector efficiency.

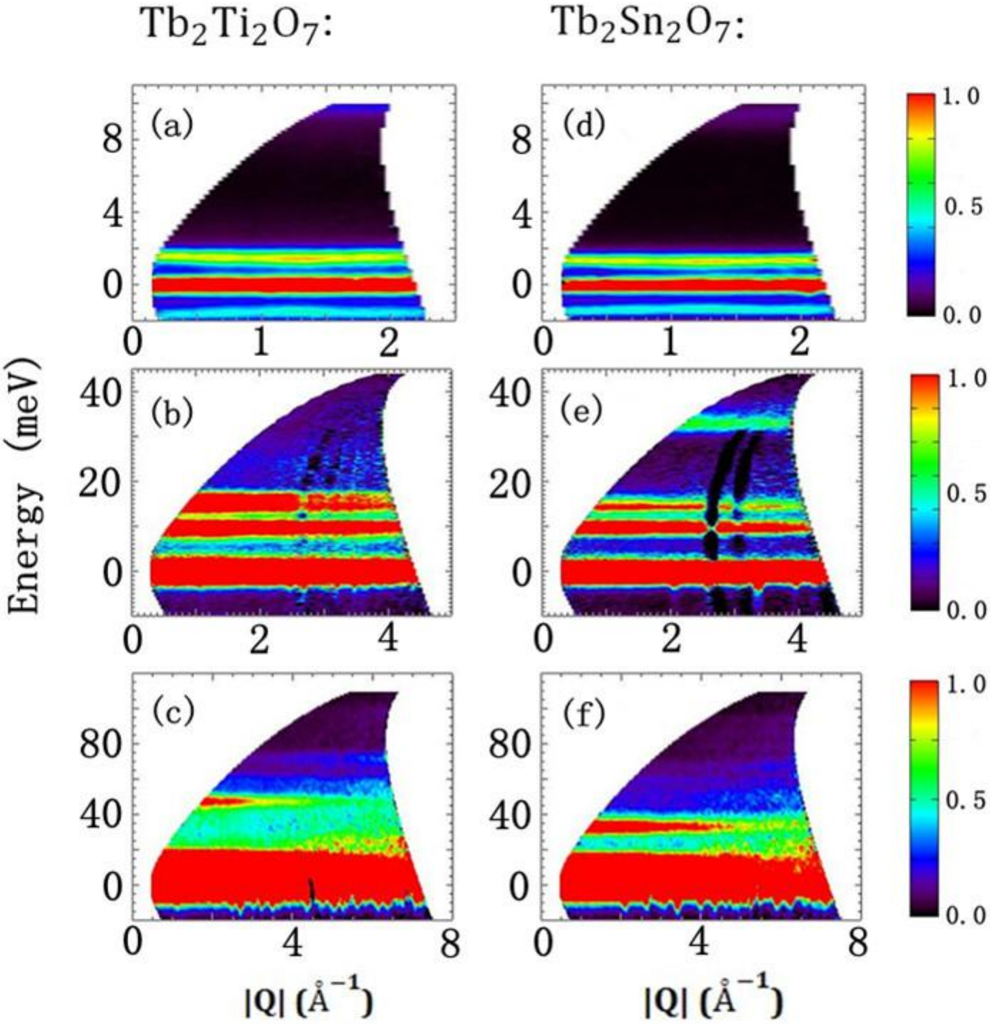

Figure 3.2: Color contour maps of energy vs |Q| from the inelastic neutron scattering data for $Tb_2Ti_2O_7$ and $Tb_2Sn_2O_7$ at T=30 K are shown. The top two plots show data at relatively low energies taken with E_i=11 meV neutrons. Well defined transitions between the ground state crystal field doublet and the lowest excited state crystal field doublet between 1-2meV without dispersion of this excitation, and de-excitation from the first excited state doublet to the ground state doublet at ~-1.5 meV are observed for both samples. The middle panel shows data up to ~43 meV, using E_i=45 meV neutrons. The bottom two plots show data taken to the highest energy transfers, using E_i=120 meV neutrons. All data sets shown are for T=30 K. An empty can background was subtracted and the data were corrected for detector efficiency.

being populated. Thus at 30 K, we observe transitions from both sets of these low lying crystal field states, but not out of the excited levels at energy >10 meV.

In Figure 3.2, we show the T=30 K inelastic neutron scattering data for $Tb_2Ti_2O_7$ (left side) and $Tb_2Sn_2O_7$ (right side) taken on the SEQUOIA time-of-flight chopper spectrometer at the SNS. Figure 3.2 a), b) and c) show data for $Tb_2Ti_2O_7$ using a) E_i=11 meV, b) E_i=45 meV, and c) E_i=120 meV, while Figure 3.2 d), e) and f) show the same E_i=11, 45, and 120 meV data sets, respectively, for $Tb_2Sn_2O_7$. These color contour maps show the full energy vs |Q| data sets. The top data sets, in Figure 3.2 a) for $Tb_2Ti_2O_7$ and Figure 3.2 d) for $Tb_2Sn_2O_7$, show the relatively low energy crystal field excitations below ~8 meV, and show great similarity between the two pyrochlores. Unlike the data sets of T=1.5 K in Figure 3.1, the lowest lying crystal field excitations, between 1 meV and 2 meV in energy, do not exhibit dispersion any more in these T=30 K data sets in both materials. Due to the first excited state being populated, the de-excitation from the first excited state doublet to the ground state doublet is observed as sharp peaks around -1.5meV for both materials. Clear differences between $Tb_2Ti_2O_7$ and $Tb_2Sn_2O_7$ are evident at intermediate energies, up to ~40 meV as seen in Figure 3.2 b) and e), and these continue to the highest energies measured, ~90 meV, as shown in Figure 3.2 c) and f).

In order to quantitatively analyze the neutron scattering results shown in Figure 3.1 in terms of appropriate crystal field excitations discussed in Section 3.2, we need to extract line scans of the intensity vs energy for data sets corresponding to each of the three E_is and for each of $Tb_2Ti_2O_7$ and $Tb_2Sn_2O_7$. Doing so requires an integration of the data in Figure 3.1 in |Q|, which depends on the energy range of interest. This is what is shown in Figure 3.3 a) for $Tb_2Ti_2O_7$ and in Figure 3.3 b) for $Tb_2Sn_2O_7$. For both materials, elastic peaks are removed and all the experimental data (blue) are normalized based on their relative intensities. We employ an integration over $1Å^{-1}$<|Q|<$1.4Å^{-1}$ for both E_i=11 meV (1-6 meV) and 45 meV (6-20 meV). The highest energy crystal field excitations extend to higher energies in $Tb_2Ti_2O_7$ compared with $Tb_2Sn_2O_7$ and consequently for the E_i=120meV data sets (20-80 meV), we employ $2Å^{-1}$<|Q|<$3Å^{-1}$ for $Tb_2Sn_2O_7$ and $2Å^{-1}$<|Q|<$5Å^{-1}$ for $Tb_2Ti_2O_7$.

Figure 3.4 a) and d) and 3.5 a) and d) show the same data at T=1.5 K (red) for a) $Tb_2Ti_2O_7$ and d) $Tb_2Sn_2O_7$, as well as the corresponding data at T=30 K (blue) for different energies. Figure 3.4 a) and d) show E_i=11 meV data from 1meV to 6meV, and the shift in the peak positions of T=1.5 K and T=30 K data results from the weak dispersion appeared in T=1.5 K data sets we discussed previously, while Figure 3.5 a) and d) show the E_i=45 meV data from 9 meV to 20 meV. Taken together Figures 3.3 a), 3.4 a) and 3.5 a) show a single transition out of the ground state at ~1meV, one transition near 10 meV, and two close together near 14 meV and 16.5 meV, a transition near 49 meV and a final very weak transition near 70 meV for $Tb_2Ti_2O_7$ at T=1.5 K. For $Tb_2Sn_2O_7$ at T=1.5 K in Figures 3.3 b), 3.4 d) and 3.5 d), we see a transition out of the ground state near 1meV, another transition near 10.5 meV, a single transition near 15.5meV, and a final observable transition at ~34 meV. For both $Tb_2Ti_2O_7$ and $Tb_2Sn_2O_7$, the general trend is that the crystal field transitions are weaker at higher energies, and thus the identification of the transitions from the ground state to the excited crystal field states is more robust at lower energies. Nonetheless, the intensity of the inelastic peaks as a function of energy can be modeled by calculations of the magnetic neutron scattering cross section appropriate to transitions between Tb^{3+} crystal field states, as described in Section 3.2.

These calculations have been carried out. In all cases we set the energy

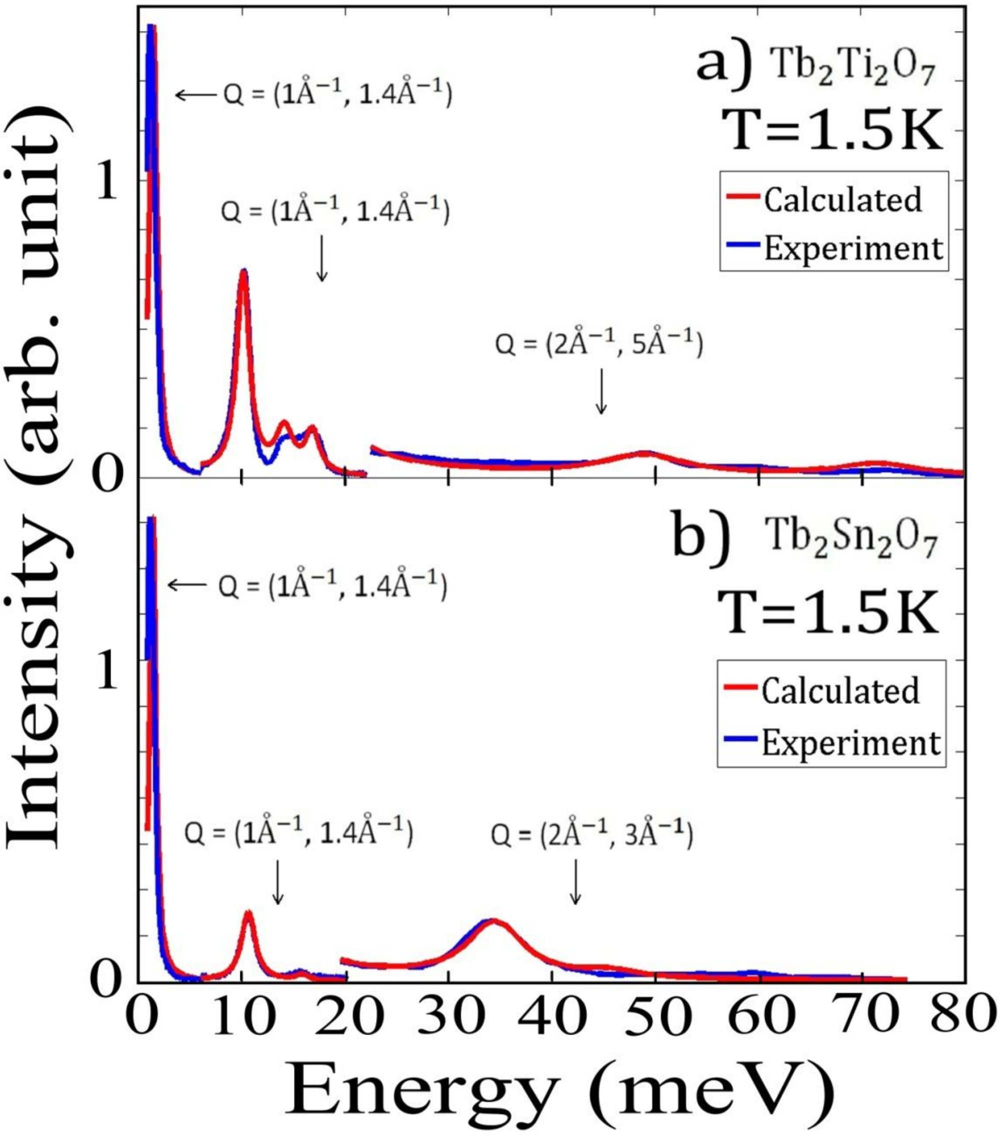

Figure 3.3: Cuts (blue) of the inelastic neutron scattering data shown in Fig. 3.1 are compared with theoertical calculations of the magnetic neutron scattering cross section for crystal field excitations from (a) $Tb_2Ti_2O_7$ and (b) $Tb_2Sn_2O_7$, at T=1.5 K. Spectra over the three different energy ranges shown in Fig. 3.3 were taken using the 3 different E_is shown in Fig. 3.1, and used an integration in |Q| as indicated in the figure.

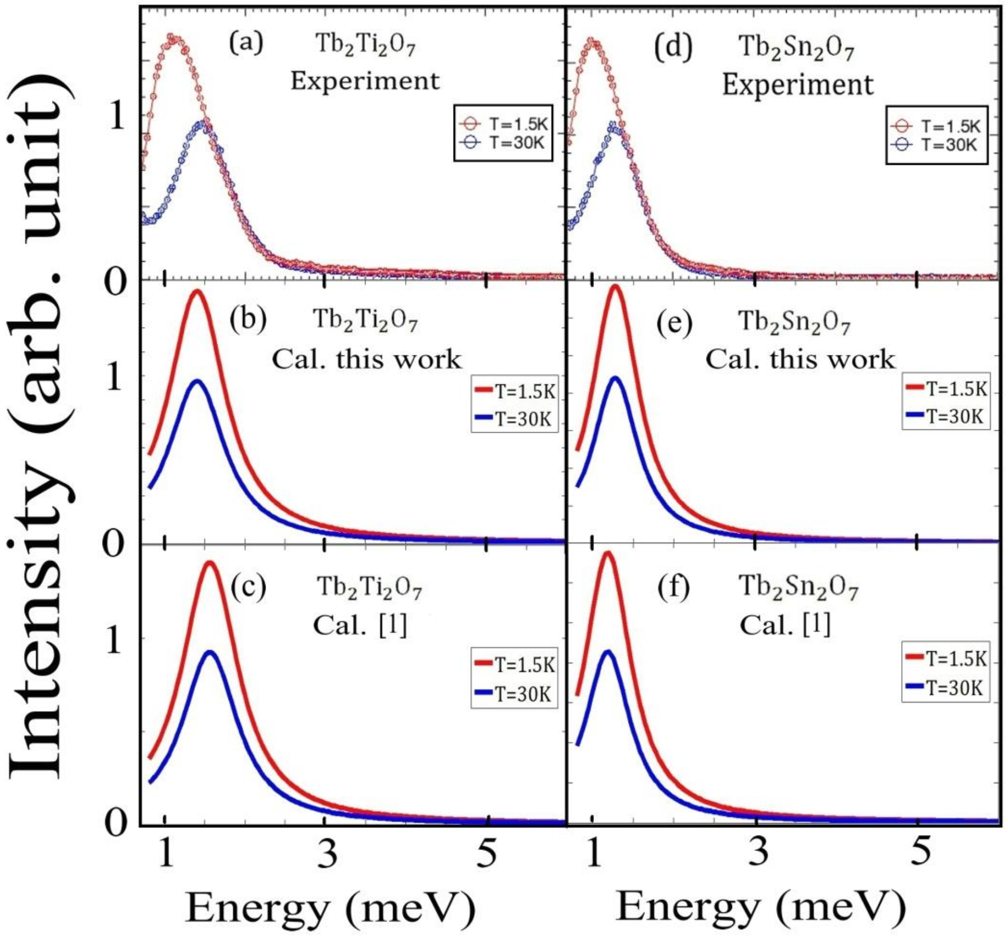

Figure 3.4: Comparison between the low energy inelastic scattering measurements (<6 meV) and calculations for the magnetic neutron scattering between crystal field states for a), b) and c) $Tb_2Ti_2O_7$ and d), e) and f) $Tb_2Sn_2O_7$. This shows the measured and calculated spectra at both T=1.5 K and T=30 K. The calculations shown in b) and d) use our newly determined crystal field parameters shown in Table 3.1. For comparison, c) and e) show the equivalent calculation using the crystal field parameters determined previously by Mirebeau *et al.* [1]. As can be seen, the temperature dependence of these low energy spectra does not distinguish between these two model calculations.

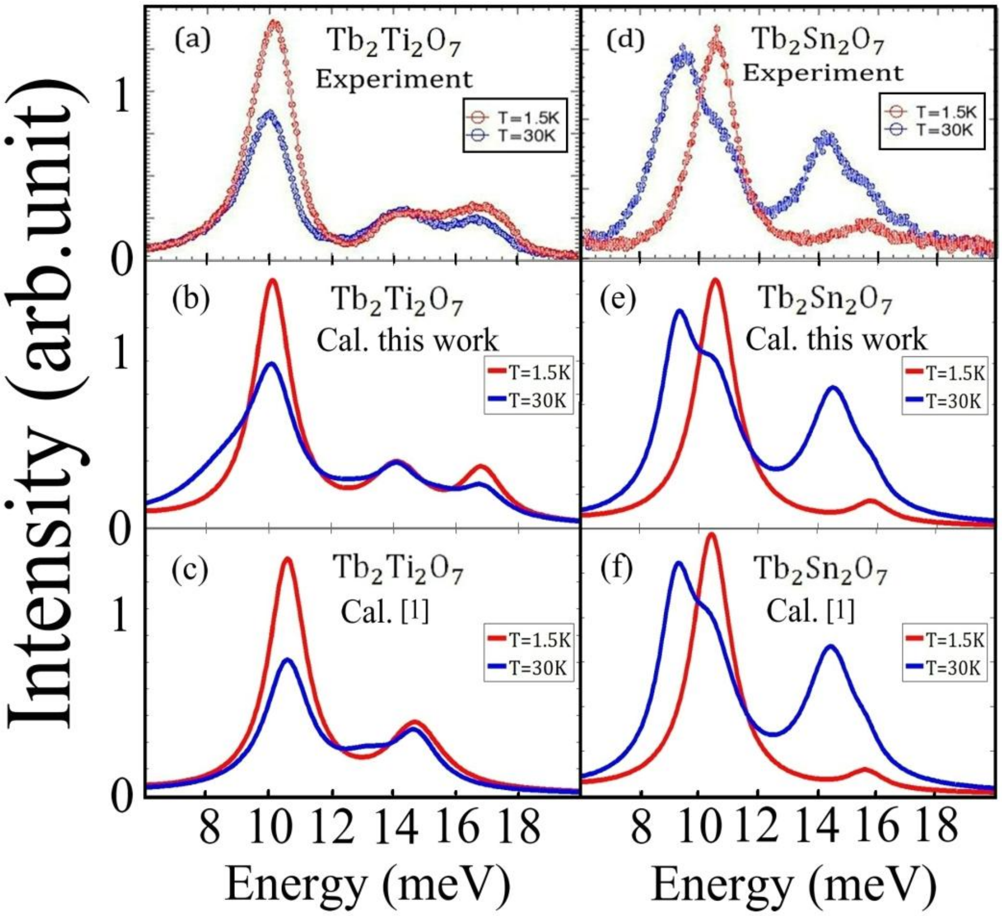

Figure 3.5: Comparison between inelastic scattering measurements at moderate energies (6 meV< energy <20 meV) and calculations for the magnetic neutron scattering between crystal field states for a), b) and c) $Tb_2Ti_2O_7$ and d), e) and f) $Tb_2Sn_2O_7$. This shows the measured and calculated spectra at both T=1.5 K and T=30 K. The calculations shown in b) and d) use our newly determined crystal field parameters shown in Table 3.1. For comparison, c) and e) show the equivalent calculation using the crystal field parameters determined previously by Mirebeau *et al.* [1]. At low temperature, T=1.5 K, this energy regime shows transitions from both the ground state doublet to crystal field states beyond the first excited state doublet. At T=30 K, it shows transitions from both the ground state doublet

and first excited state doublet to crystal field states beyond the first excited state doublet. For that reason, and in contrast to data shown in Fig. 3.4, this inelastic data is very sensitive to the specific details of the eigenfunctions of both the ground state and first excited state doublet.

widths associated with all transitions, $\Gamma_{\lambda\lambda'}$ to be determined by our finite energy resolution of ~3% of E_i, so full widths at half maximum of ~0.3meV for $E_i = 11\,\text{meV}$, 1.4 meV for $E_i = 45\,\text{meV}$ and 3.6 meV for $E_i = 120\,\text{meV}$. This calculation will not reproduce the dispersion known to be relevant to the lowest ~1.5 meV transitions at T=1.5 K, in both materials, as shown in Figure 3.4 a) and d). For that reason, we fitted the integrated intensity of this lowest transition, artificially raised in energy to their T=30 K value.

In the case of $Tb_2Sn_2O_7$ we used the crystal field parameters previously determined for $Tb_2Sn_2O_7$ by Mirebeau and co-workers as starting points to fit our spectra [1]. In the case of $Tb_2Ti_2O_7$, we also used the Mirebeau *et al.* [1] parameters previously determined for $Tb_2Ti_2O_7$, but minimized both the sum of the least squares of the difference between the measured and calculated neutron intensity, as well as the sum of the least squares of the difference between the experimental and calculated crystal field enegies. In the case of $Tb_2Ti_2O_7$, this was required in order to place two excitations from the ground state doublet to excited states in the 12-17 meV energy range, as observed in the data reported here, and also in earlier measurements on $Tb_2Ti_2O_7$.

However the crystal field calculation using the $Tb_2Ti_2O_7$ parameters determined by Mirebeau *et al.* [1] produces only a single crystal field level in this same energy regime. For this reason, and as shown explicitly in Figure 3.5 c), the $Tb_2Ti_2O_7$ calculated parameters determined from Mirebeau *et al.* [1] are not a good starting point for the full description of our $Tb_2Ti_2O_7$ inelastic neutron scattering spectra. In contrast, the Mirebeau *et al.* parameters for $Tb_2Sn_2O_7$ are a good starting point to describe our $Tb_2Sn_2O_7$ neutron data, as shown in Figure 3.5 f).

The results of this fitting procedure are shown as the red lines in Figure 3.3 a) and b) for $Tb_2Ti_2O_7$ and $Tb_2Sn_2O_7$, respectively, and in Figure 3.4 b) and

3.5 b) for $Tb_2Ti_2O_7$ at T=1.5 K (red) and 30 K (blue), as well as Figure 3.4 e) and 3.5 e) for $Tb_2Sn_2O_7$ at T=1.5 K (red) and 30 K (blue). Clearly the description of the crystal field excitation energies and intensities is very good over the full energy range studied for both $Tb_2Ti_2O_7$ and $Tb_2Sn_2O_7$. We also repeated this same fitting procedure for both materials using a variable energy width, $\Gamma_{\lambda\lambda'}$, for each transition. While this produced better agreement between the measured and calculated neutron spectra than fitting with $\Gamma_{\lambda\lambda'}$ fixed at values approximating the finite energy resolution of the spectrometer, it did not affect the eigenvalues or eigenfunctions extracted from these fits at the 2% level.

It is clear from Figure 3.4 a) and d) that the low energy crystal field eigenvalues are very similar in $Tb_2Ti_2O_7$ and $Tb_2Sn_2O_7$ at both T=1.5 K and T=30 K. The mean energy and the weak dispersion characterizing the transition from the ground state to first excited state are both very similar in the two materials. It is at higher energies, in particular between 6 meV and 20 meV, as shown in Figure 3.5 a) and d), where significant qualitative differences appear. Specifically, at T=1.5 K, $Tb_2Ti_2O_7$ shows three transitions from the ground state to excited crystal field states in this range, while $Tb_2Sn_2O_7$ shows only two. This difference, clear in both the T=1.5 K data sets of Figure 3.5 a) and d), and in the very different temperature dependence which occurs on populating the first set of excited states, as occurs for either material at T=30 K, was not fully appreciated in earlier triple axis neutron spectroscopic studies of the Tb^{3+} levels in $Tb_2Ti_2O_7$ [1,7] and $Tb_2Sn_2O_7$ [1]. The first such work, by Gingras *et al.*. [7] on $Tb_2Ti_2O_7$ was performed at T=12 K, and consequently the “extra” peak near 14 meV was misinterpreted as arising out of the first excited state, rather than out of the ground state. The later work by Mirebeau *et al.* [1] on $Tb_2Ti_2O_7$ did show a discrepancy between triple axis neutron measurements and the corresponding crystal field calculation, but this discrepancy was not refined such that three excitations at T=1.6 K, from the ground state doublet of $\mathrm{Tb_2Ti_2O_7}$ to excited crystal field states in the 6-20 meV range could be accounted for.

Our new fits to our new $\mathrm{Tb_2Ti_2O_7}$ data in this range, shown in Figure 3.5 a) and b), are an excellent description of this data at T=1.5K. At T=30 K, the description is also good, although a weak excitation arising from a transition from the excited state doublet to a singlet, ~10 meV above the ground state is not as evident in the data (Figure 3.5 a)) as the calculation (Figure 3.5 b)) predicts. There is a small shift towards lower energies in the peak near 10 meV at 30 K compared with 1.5 K, and the lineshape is asymmetric with enhanced scattering on the lower energy side, consistent with an additional peak on the low energy shoulder of the ~10 meV peak at T=30 K. However the observed effect is less pronounced than the calculation. This could arise because this excitation out of the excited state doublet has either dispersion or a finite lifetime, and therefore has a larger energy width than that which we have ascribed to it on the basis of energy resolution alone. Indeed, the aforementioned fits in which the $\Gamma_{\lambda\lambda'}$ is a fit parameter account for this effect well.

The six crystal field parameters, $\mathrm{D_n^m}$, arising from this fitting procedure for $\mathrm{Tb_2Ti_2O_7}$ and $\mathrm{Tb_2Sn_2O_7}$ are listed in Table 3.1 (in $\mathrm{cm^{-1}}$~0.12 meV). This set of parameters describes very well the transitions out of the ground state (at T=1.5 K) shown in Figure 3.3 and Figures 3.4 and 3.5, as well as out of the equilibrium population of ground state and first excited state appropriate to 30 K. Given that the first excited state is at ~1.5 meV at 30 K and the next highest energy crystal field state is at ~10 meV ~110 K, both the ground state and first excited states in both $\mathrm{Tb_2Ti_2O_7}$ and $\mathrm{Tb_2Sn_2O_7}$ are approximately equally populated at T=30 K. The calculation of the magnetic neutron scattering in the low energy regime, with transitions between the ground state

Table 3.1: Crystal field parameters ($\mathrm{D_n^m}$) appropriate to $\mathrm{Tb^{3+}}$ in $\mathrm{Tb_2Ti_2O_7}$ and $\mathrm{Tb_2Sn_2O_7}$ as derived from fitting our inelastic neutron scattering data at both T=1.5 K and 30 K with calculations of the magnetic neutron scattering cross section due to transitions between crystal field states.

	D_2^0 (cm^{-1})	D_4^0 (cm^{-1})	D_4^3 (cm^{-1})	D_6^0 (cm^{-1})	D_6^3 (cm^{-1})	D_6^6 (cm^{-1})
$Tb_2Ti_2O_7$	582.6	272.3	3890.1	86.7	3624.4	6159.1
$Tb_2Sn_2O_7$	157.6	232.1	1713	-20.4	-434	839.1

and first excited state only is shown in Figure 3.4. The intensity of this transition drops by a factor of ~ two between T=1.5 K and T=30 K for any model which possesses the same degeneracy for the ground state and first excited state, which is the case for both our crystal field parameters shown in Table 3.1 and those obtained earlier by Mirebeau and co-workers [1]. Thus the temperature dependence of the low energy crystal field scattering is not a sensitive probe of the nature of the $\mathrm{Tb^{3+}}$ crystal field parameters in either material. However, the temperature dependence of the crystal field scattering at higher energies, as shown between 6 meV and 20 meV in Figure 3.5, such that one can also probe transitions from the first excited state, which is populated at 30 K, is much richer. Here one is very sensitive to the details of the ground state and first excited state eigenfunctions, as well as to the details of the eigenfunctions relevant to the high energy crystal field states which the neutron can make transitions to.

3.4 Discussion

The resulting energy eigenvalues and eigenfunctions arising from fitting our inelastic neutron scattering data on $\mathrm{Tb_2Ti_2O_7}$ and $\mathrm{Tb_2Sn_2O_7}$ are given in Table 3.2. The first column shows the energy of the state for $\mathrm{Tb_2Ti_2O_7}$ (top) and $\mathrm{Tb_2Sn_2O_7}$ (bottom), and the corresponding eigenstate of each eigenvalue in terms of $\mathrm{J_z}$ basis is given behind the eigenvalues. The non-scaled spectra of energy eigenvalues is illustrated in Figure 3.6. As was clear from our earlier discussion, and consistent with earlier measurements, the lowest energy sector consists of a ground state doublet and first excited state doublet separated by an energy ~1.5 meV in both materials. However, the eigenfunctions making these doublets are quite different. In the case of $\mathrm{Tb_2Sn_2O_7}$, our results are consistent with early triple axis work [1], wherein the ground state (g) and first excited state (1) doublet contain predominantly $\mathrm{J_z} = |\mp 5>$ and $\mathrm{J_z} = |\mp 4>$ respectively, and are fully described by (round off to the third decimal place):

$$\left|\psi_g^{\mathrm{Sn}}\right>= 0.925\left|\mp 5> \pm 0.292|\pm 4> \pm 0.242|\mp 2> +0.017|\pm 1> \right. \quad (3.5)$$

and

$$\left|\psi_1^{\mathrm{Sn}}\right>= 0.942\left|\mp 4> \pm 0.300|\pm 5> \pm 0.149|\mp 1> +0.020|\pm 2> \right. \quad (3.6)$$

For $\mathrm{Tb_2Ti_2O_7}$ however, our new eigenfunctions are very different from those previously reported [1,8]. The ground state doublet corresponds to a significant mixture of $\mathrm{J_z} = |\mp 5>, \mathrm{J_z} = |\pm 4>\ and\ \mathrm{J_z} = |\mp 2>$, while the first excited state doublet corresponds to a mixture of $\mathrm{J_z} = |\pm 4>, \mathrm{J_z} = |\mp 5>\ and\ \mathrm{J_z} = |\pm 1>$. They are fully written as:

$$\left|\psi_g^{\mathrm{Ti}}\right>= 0.810\left|\mp 5> \pm 0.472|\pm 4> \pm 0.338|\mp 2> +0.078|\pm 1> \right. \quad (3.7)$$

and

$$\left|\psi_1^{\mathrm{Ti}}\right>= 0.799\left|\pm 4> \mp 0.507|\mp 5> \mp 0.279|\pm 1> +0.163|\mp 2> \right. \quad (3.8)$$

For reference, we have calculated the magnetic neutron scattering spectra

Table 3.2: The crystal field eigenvalues and eigenstates determined for Tb^{3+} in $Tb_2Ti_2O_7$ (top) and $Tb_2Sn_2O_7$ (bottom) are shown. The first column displays all of the crystal field energy eigenvalues, while the corresponding eigenfunction appropriate to each eigenvalue is given in each such row, in terms of the J_z basis states for J=6.

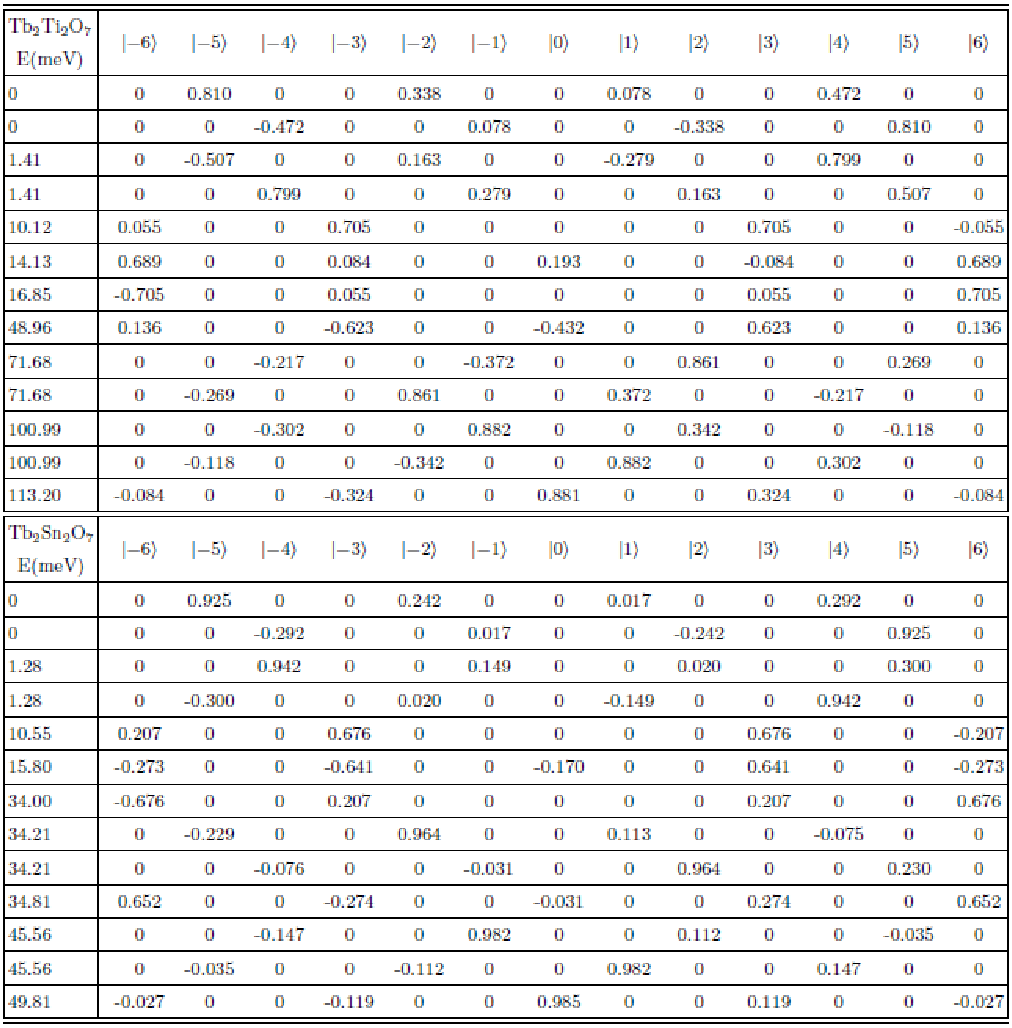

$Tb_2Ti_2O_7$ E(meV)	$\vert -6\rangle$	$\vert -5\rangle$	$\vert -4\rangle$	$\vert -3\rangle$	$\vert -2\rangle$	$\vert -1\rangle$	$\vert 0\rangle$	$\vert 1\rangle$	$\vert 2\rangle$	$\vert 3\rangle$	$\vert 4\rangle$	$\vert 5\rangle$	$\vert 6\rangle$
0	0	0.810	0	0	0.338	0	0	0.078	0	0	0.472	0	0
0	0	0	-0.472	0	0	0.078	0	0	-0.338	0	0	0.810	0
1.41	0	-0.507	0	0	0.163	0	0	-0.279	0	0	0.799	0	0
1.41	0	0	0.799	0	0	0.279	0	0	0.163	0	0	0.507	0
10.12	0.055	0	0	0.705	0	0	0	0	0	0.705	0	0	-0.055
14.13	0.689	0	0	0.084	0	0	0.193	0	0	-0.084	0	0	0.689
16.85	-0.705	0	0	0.055	0	0	0	0	0	0.055	0	0	0.705
48.96	0.136	0	0	-0.623	0	0	-0.432	0	0	0.623	0	0	0.136
71.68	0	0	-0.217	0	0	-0.372	0	0	0.861	0	0	0.269	0
71.68	0	-0.269	0	0	0.861	0	0	0.372	0	0	-0.217	0	0
100.99	0	0	-0.302	0	0	0.882	0	0	0.342	0	0	-0.118	0
100.99	0	-0.118	0	0	-0.342	0	0	0.882	0	0	0.302	0	0
113.20	-0.084	0	0	-0.324	0	0	0.881	0	0	0.324	0	0	-0.084

$Tb_2Sn_2O_7$ E(meV)	$\vert -6\rangle$	$\vert -5\rangle$	$\vert -4\rangle$	$\vert -3\rangle$	$\vert -2\rangle$	$\vert -1\rangle$	$\vert 0\rangle$	$\vert 1\rangle$	$\vert 2\rangle$	$\vert 3\rangle$	$\vert 4\rangle$	$\vert 5\rangle$	$\vert 6\rangle$
0	0	0.925	0	0	0.242	0	0	0.017	0	0	0.292	0	0
0	0	0	-0.292	0	0	0.017	0	0	-0.242	0	0	0.925	0
1.28	0	0	0.942	0	0	0.149	0	0	0.020	0	0	0.300	0
1.28	0	-0.300	0	0	0.020	0	0	-0.149	0	0	0.942	0	0
10.55	0.207	0	0	0.676	0	0	0	0	0	0.676	0	0	-0.207
15.80	-0.273	0	0	-0.641	0	0	-0.170	0	0	0.641	0	0	-0.273
34.00	-0.676	0	0	0.207	0	0	0	0	0	0.207	0	0	0.676
34.21	0	-0.229	0	0	0.964	0	0	0.113	0	0	-0.075	0	0
34.21	0	0	-0.076	0	0	-0.031	0	0	0.964	0	0	0.230	0
34.81	0.652	0	0	-0.274	0	0	-0.031	0	0	0.274	0	0	0.652
45.56	0	0	-0.147	0	0	0.982	0	0	0.112	0	0	-0.035	0
45.56	0	-0.035	0	0	-0.112	0	0	0.982	0	0	0.147	0	0
49.81	-0.027	0	0	-0.119	0	0	0.985	0	0	0.119	0	0	-0.027

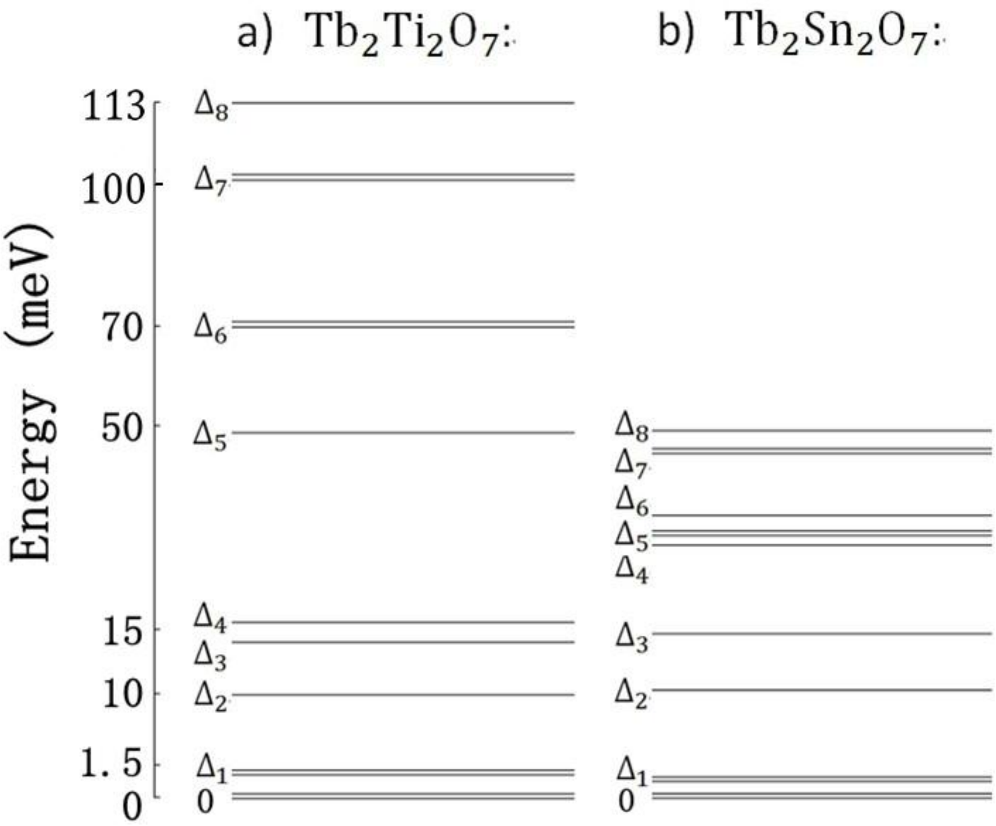

Figure 3.6: Crystal field energy scheme for all the (2J+1)=13 levels for Tb^{3+} in (a) $Tb_2Ti_2O_7$ and (b) $Tb_2Sn_2O_7$, as derived from our calculations of the magnetic neutron scattering cross section from transitions between crystal field states are shown (not to scale). These calculations employed the best-fit crystal field parameter sets determined for $Tb_2Ti_2O_7$ and $Tb_2Sn_2O_7$ shown in Table 3.1.

using the crystal field parameters obtained earlier by Mirebeau *et al.* [1], and these results are compared to our new experimental data in Figures 3.4 c) and e) and Figures 3.5 c) and e). It is only for $Tb_2Ti_2O_7$ and only for the crystal field levels in the 6 to 20 meV range, shown in Figure 3.5 c), that the deficiency of the earlier estimate for the crystal field parameters is evident. This earlier work misses a transition peak at ~16 meV. We note that earlier still triple axis work by Gingras *et al.* [7], which reached much the same conclusions as that of Mirebeau *et al.* [1], did not produce estimates for the D_n^m crystal field parameters, and we could not easily perform the equivalent comparision of earlier theory to our new experiment.

We note that Figure 3.6, which illustrates the dynamic range of the splitting of the (2J+1)=13 crystal field levels in $Tb_2Ti_2O_7$ and $Tb_2Sn_2O_7$, makes it clear that the overall scale or bandwidth for the crystal field splitting is a factor of ~2 greater in $Tb_2Ti_2O_7$ compared with $Tb_2Sn_2O_7$. There are two free parameters within the $Fd\bar{3}m$ space group which $Tb_2Ti_2O_7$ and $Tb_2Sn_2O_7$ share: the cubic lattice parameter and the oxygen position parameter, x, which determines the positions of six of the eight oxygen ions in the immediate vicinity of the Tb^{3+} ion. It is the cubic lattice parameter which increases at room temperature from $Tb_2Ti_2O_7$ (a=10.149Å) to $Tb_2Sn_2O_7$ (a=10.426Å) which is largely responsible for the fact that the overall bandwidth of the crystal field splitting is smaller in $Tb_2Sn_2O_7$ compared with $Tb_2Ti_2O_7$. While such an effect is expected, nonetheless, its scale is remarkably large.

Our newly determined eigenfunctions for the ground state and first excited crystal field state doublets in $Tb_2Ti_2O_7$ are more similar to those appropriate to $Tb_2Sn_2O_7$ than previously thought. As shown in Equations 3.5 and 3.6, and Table 3.2, the ground state doublet in $Tb_2Sn_2O_7$ remains primarily $J_z = |\mp 5>$, while the first excited state doublet remains primarily $J_z = |\mp 4>$. For $Tb_2Ti_2O_7$, the ground state and first excited state doublets are now determined to be a more equitable mixture of the symmetry allowed J_z basis states, but the largest component remains $J_z = |\mp 5>$ for the ground state and $J_z = |\pm 4>$ for the first excited state doublets.

While the exchange interactions between Tb^{3+} rare earth moments are very likely to be anisotropic in nature, as was determined recently for both $Yb_2Ti_2O_7$ [11] and $Er_2Ti_2O_7$ [12], the differences between the microscopic Hamiltonians in $Tb_2Ti_2O_7$ and $Tb_2Sn_2O_7$ are likely to be subtle. $Tb_2Ti_2O_7$ has the more antiferromagnetic θ_{CW} and its ground state moment should be slightly smaller than that of $Tb_2Sn_2O_7$, a consequence of mixing of small J_z basis states into the eigenfunction of the ground state doublet. The smaller magnetic moment translates into weaker dipolar interactions. As near-neighbour dipolar interactions on the pyrochlore lattice are effectively ferromagnetic in nature, both of these effects will tend to make $Tb_2Sn_2O_7$ closer to the expectations of a spin ice ground state. Recent neutron experiments are now showing a disordered, frozen antiferromagnetic spin ice state in $Tb_2Ti_2O_7$ at very low temperatures in zero field. Therefore both materials exhibit a variant of the spin ice ground state at sufficiently low temperatures, which is consistent with the similarities between their structures, low lying crystal field states, and their interactions as quantified through their Θ_{CW}.

3.5 Conclusion

We have performed new time-of-flight inelastic neutron scattering spectroscopy of the crystalline electric field states of Tb^{3+} in $Tb_2Ti_2O_7$ and $Tb_2Sn_2O_7$. These measurements probe transitions out of the ground state doublet alone at T=1.5 K, as well as out of the equilibrium distribution of the ground state and first excited state doublet at T=30 K. We use these magnetic excitation spectra to produce a robust determination of the eigenvalues and eigenfunctions appropriate to the (2J+1)=13 crystal field states appropriate to the J=6 Tb^{3+} magnetic moments in these materials. Our results for $Tb_2Sn_2O_7$ are consistent with a previous determination of these eigenfunctions and eigenvalues, for which the ground state doublet is principally comprised of the $J_z = |\mp 5 >$ basis states, while the first excited state is principally comprised of the $J_z = |\mp 4 >$ basis states. Our results for $Tb_2Ti_2O_7$ are not consistent with previous estimates, mainly due to a previously mis-identified transition from the ground state doublet near 14meV. Our new determination of the ground state and 1st excited state eigenfunctions in $Tb_2Ti_2O_7$ show them to be made up of a distribution of the symmetry allowed J_z basis states, where the largest contribution to the ground state doublet comes from $J_z = |\mp 5 >$, and the largest contribution to the first excited state doublet comes from $J_z = |\pm 4 >$. The detailed eigenfunctions and eigenvalues for $Tb_2Ti_2O_7$ and $Tb_2Sn_2O_7$ are listed in Table 3.2 and illustrated in Figure 3.6.

These results show the bandwidth of the energy eigenvalues to be a remarkable factor of ~2 greater in $Tb_2Ti_2O_7$ compared with $Tb_2Sn_2O_7$. This is qualitatively consistent with the fact that the cubic pyrochlore lattice is slightly expanded in $Tb_2Sn_2O_7$ compared with $Tb_2Ti_2O_7$.

Finally, we note that the precise nature of the low lying crystal field levels is central to both theoertical proposals which have been put forward to explain the lack of magnetic order in $Tb_2Ti_2O_7$ to temperatures much less than 1 K. Our results will contribute to the construction of a more precise theoretical model of $Tb_2Ti_2O_7$, which is vital to the potential resolution of the debate of the nature of this ground state.

Bibliography

1. I. Mirebeau, P. Bonville, and M.Hennion, Phys. Rev. B **76**, 184436 (2007)
2. M.P. Zinkin, M.J.Harris, Z. Turn, R.A. Cowley and B.M. Wanklyn, J. Phys.: Condens. Matter **8**, 193 (1996)
3. R. Siddharthan, B.S. Shastry, A.P. Ramirez, A. Hayashi, R.J. Cava and S. Rosenkranz, Phys. Rev. Lett. **83**, 1854 (1999)
4. J.D.M. Champion, M.J. Harris, P.C.W. Holdsworth, A.S. Wills, G. Balakrishnan, S.T. Bramwell, E. Cizmar, T. Fennell, J.S. Gardner, J. Lago, D.F. McMorrow, M. Orendac, A. Orendacova, D. McK. Oaul, R.I. Smith, M.T.F. Telling and A. Wildes, Phys. Rev. B **68**, 020401 (2003)
5. J.S. Gardner and G. Ehlers, J. Phys.: Condens. Matter **21**, 436004 (2009)
6. A. Bertin, Y. Chapuis, P. Dalmas de Reotier and A. Yaouanc, J. Phys.: Condens. Matter **24,** 256003 (2012)
7. M. J. Gingras, B. C. den Hertog, M. Faucher, J.S. Gardner, S. R. Dunsiger, L. J. Chang, B. D. Gaulin, N. P. Raju. and J. E. Greedan, Phys. Rev. B **62**, 6496 (2000)
8. J. S. Gardner, B. D. Gaulin, A. J. Berlinsky, and P. Waldron, Phys. Rev. B, **64**, 224416, (2001)

9. J.S. Gardner, S.R. Dunsiger, B.D. Gaulin, M.J.P. Gingras, J.E. Greedan, R.F. Kiefl, M.D. Lumsden, W.A. MacFarlane, N.P. Raju, J.E. Sonier, I. Swainson and Z. Tun, Phys. Rev. Lett. **82**, 1012 (1999)

10. M. Kanada, Y. Yasui, M. Ito, H. Harashina, M. Sato, H. Okumura and K. Kakurai, J. Phys. Soc. Japan **68,** 3802 (1999)

11. K.A. Ross, L. Savary, B.D. Gaulin, and L. Balents, Phys. Rev. X **1**, 021002 (2011)

12. L. Savary, K.A. Ross, B.D. Gaulin, J.P.C. Ruff, and L. Balents, Phys. Rev. Lett. **109**, 167201 (2012)

Chapter 4

Crystal Field Disorder in the Quantum Spin Ice Ground State of $Tb_2Sn_{2-x}Ti_xO_7$

4.1 Introduction

The contents of this chapter are based on a manuscript which is in preparation for submission to publication. I wish to emphasize that only the neutron scattering work is done by myself with the help of my supervisor and students within this group. The μSR data and AC magnetic susceptibility data are provided by our experimental collaborators, Philippe Mendels's and Fabrice Bert's groups and Peter Schiffer' s group, respectively.

Here again, I would like to mention and acknowledge many people's help in the work of this chapter. First, I wish to thank Prof. Cava's group in the Department of Chemistry at Princeton University for the synthesis of the samples. Second, I wish to thank Katharina Fritsch and Bruce Gaulin for their help while we were doing the neutron scattering measurements in Oak Ridge National Lab in May, 2012. Finally, I would like to thank my supervisor, Bruce Gaulin, as he and I co-wrote most of the content in this chapter as part of a manuscript which is being prepared for submission to publication.

Having determined the crystal field states in $Tb_2Ti_2O_7$ and $Tb_2Sn_2O_7$ in Chapter 3, in this chapter, we will study a series of related solid solutions

$Tb_2Sn_{2-x}Ti_xO_7$ through three different experiment methods: Inelastic neutron scattering, AC magnetic susceptibility and Muon spin relaxation (μSR). Starting from a "soft" spin ice ground state at x=0, $Tb_2Sn_2O_7$ eventually morphs into a quantum spin ice ground state at x=2, $Tb_2Ti_2O_7$. These experimental studies present useful information regarding the transformation from one type of ground state to the other. These measurements help us probe the crystal field states, low energy spin dynamics and phase transitions of $Tb_2Sn_{2-x}Ti_xO_7$ as well as how the system evolves in doping. To sum up, it shows a novel, dynamic spin liquid state for all x other than the two end members x=0, $Tb_2Sn_2O_7$ and x=2, $Tb_2Ti_2O_7$ which are, respectively, ordered spin ice and quantum spin ice ground states. The magnetic order in x=0, $Tb_2Sn_2O_7$, is quite delicate and absent even for x=0.1. It shows a greatly enhanced spin dynamics at low energies and a mixing of low lying crystal field levels for intermediate concentrations. At high crystal field energies, we observe a remarkable electronic homogeneity in $Tb_2Sn_{2-x}Ti_xO_7$.

The experimental details are as follows.

Polycrystaline samples of $Tb_2Sn_{2-x}Ti_xO_7$ were prepared by mixing high purity Tb_4O_7, TiO_2 and SnO_2 starting materials in the appropriate stoichiometric ratios and placing them in high density aluminum oxide crucibles. The samples were heated in air for two day periods, with intermediate grinding, at temperatures of 1100, 1200, 1300 and finally 1350 ℃, where several heating and grinding cycles were repeated until the materials were single phase and displayed high quality powder X-ray diffraction patterns.

Inelastic neutron scattering measurements were performed on the SEQUOIA direct geometry time-of-flight spectrometer at the Spallation Neutron Source of Oak Ridge National Laboratory. Powder samples were placed in a flat plate Al cell to completely cover the 5cm×5cm beam. Seven samples were measured: x=0, x=0.1, x=0.2, x=0.5, x=1, x=1.5 and x=2. They were all measured with two temperatures: T=1.5 K and T=30 K. Measurements were performed over a wide dynamic range of energies by using three incident neutron energies, E_i, of 11 meV, 45 meV and 120 meV. The lower incident energy is employed to probe the low energy spin dynamics while the higher incident energies are employed to cover a larger dynamic range in energy and probe the higher energy crystal field excitations. The energy resolution is about 2-3% of E_i. Every measurement was carried out for two hours of counting time and measurements with an empty aluminum can were performed so that the background data can be subtracted from the signal of every measurement.

Different incident neutron energies were selected by using different combinations of frequencies of the Fermi chopper and the T_0 chopper. Two 100 mm in diameter Fermi choppers were used for these measurements: the coarse resolution chopper had a 3.5 mm slit spacing used for E_i=120 meV with a spin frequency of 300 Hz, and the fine resolution chopper had a 2 mm slit spacing used for E_i=11 meV and 45 meV with spin frequencies of 180 Hz and 420 Hz respectively. Meanwhile, the T_0 chopper spun at 60 Hz for E_i=11 meV, at 90 Hz for E_i=45 meV, and at 180 Hz for E_i=120 meV.

4.2 Neutron Scattering Measurements

For all the seven samples of $Tb_2Sn_{2-x}Ti_xO_7$, nearly identical amounts of the powder samples were loaded into identical sample cans in the same cryostat, such that direct comparisons can be made between these sets of data from different samples.

Figure 4.1 shows color contour maps of the inelastic neutron scattering data for 7 concentrations of $Tb_2Sn_{2-x}Ti_xO_7$ at T=1.5 K. The seven measurements were all taken with E_i=11 meV neutrons in order to get low energy, high resolution data below ~8 meV. As was shown in last chapter, for the two end members, x=0 and x=2, great similarity can be observed. Well defined low energy crystal field excitations between the ground state doublet and the lowest excited state doublet appear as sharp peaks in energy between 1-2 meV with weak dispersion, displaying a minimum around |Q|~1.25 $Å^{-1}$ for both cases [1-3]. This dispersive behavior disappears in our T=30 K data sets shown later. Well defined crystal field excitations are lost at all wavevectors for all concentrations except for the two end members, x=0 and x=2. For the most lightly disordered x=0.1 and x=0.2 samples, some enhanced spectral weight concentrated in energy between 1-2meV can be observed. Remarkably for the intermediate concentrations x=0.5, 1 and 1.5, we see a much broader bandwidth of low energy magnetic scattering extending to about 3× the energy of first crystal field excitations in either $Tb_2Ti_2O_7$ or $Tb_2Sn_2O_7$.

Now let’s turn our attention to measurements at higher temperatures. Figure 4.2 shows color contour maps of the inelastic neutron scattering data for the same 7 concentrations of $Tb_2Sn_{2-x}Ti_xO_7$ taken with E_i=11meV neutrons but at T=30 K. For the T=1.5 K case, only the ground state is occupied while for the T=30 K case, both the ground state and first excited state are occupied based on the expected Maxwell–Boltzmann distribution. Compared with the T=1.5 K data sets, some similarities can be observed in T=30 K data sets such as the well defined low energy crystal field excitations between the ground state doublet and the lowest excited state doublet in the two end members, and the absence of this transition replaced by a broad distribution of low energy scattering in the intermediate concentration samples. However, some new features can be observed in these T=30 K data sets, mainly in the two end samples. The dispersive behavior disappears and the de-excitation from the

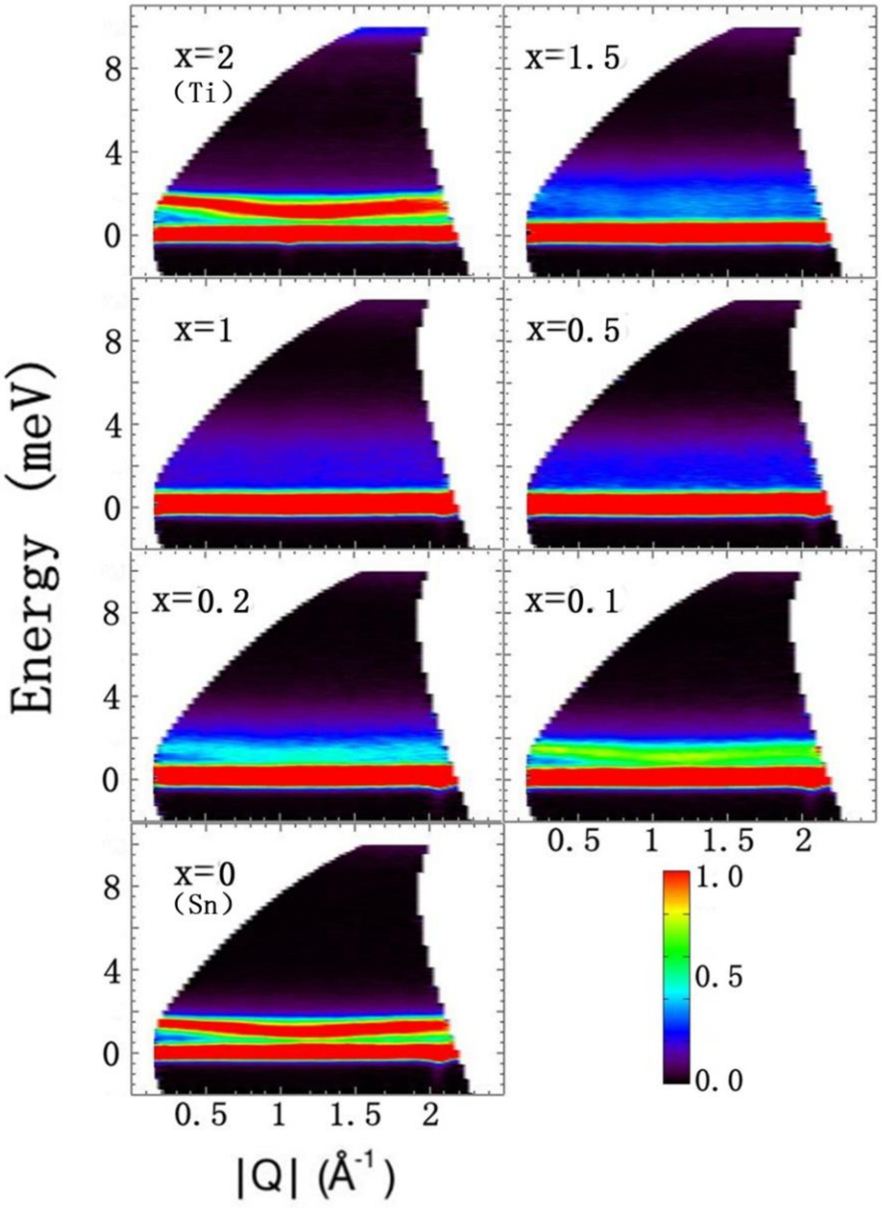

Figure 4.1: Color contour plots of the inelastic neutron scattering data for 7 concentrations of $Tb_2Sn_{2-x}Ti_xO_7$ at T=1.5 K with E_i=11 meV neutrons are shown. Well defined transitions between the ground state CF doublet and the lowest excited CF doublet near 1.5meV with weak dispersion are observed for the end members $Tb_2Sn_2O_7$, x=0, and $Tb_2Ti_2O_7$, x=2, while intermediate concentrations show the absence of the transitions and see a much broader bandwidth to these low energy spin dynamics.

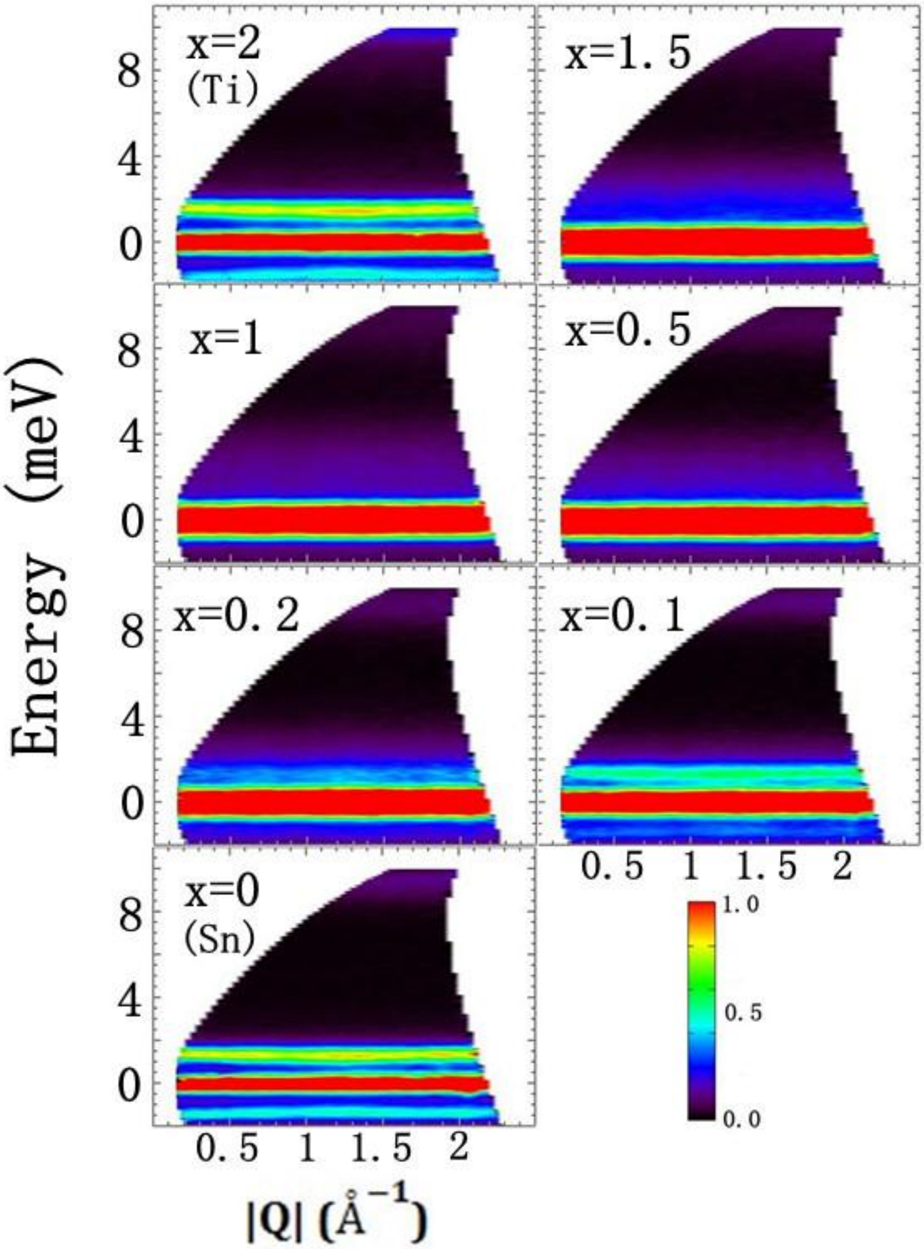

Figure 4.2: Color contour plots of the inelastic neutron scattering data for 7 concentrations of $\mathrm{Tb_2Sn_{2-x}Ti_xO_7}$ at T=30 K with E_i=11 meV neutrons are shown. Similarly to the T=1.5K data, well defined transitions between the ground state CF doublet and the lowest excited CF doublet near 1.5meV but with dispersionless are observed for the end members $\mathrm{Tb_2Sn_2O_7}$, x=0, and $\mathrm{Tb_2Ti_2O_7}$, x=2, while intermediate concentrations show the absence of the

transitions and see a much broader bandwidth to these low energy spin dynamics. Furthermore, de-excitation from first excited CF doublet to the ground state CF doublet near -1.5 meV are observed for the end members $\mathrm{Tb_2}Sn_2\mathrm{O_7}$, x=0, and $\mathrm{Tb_2Ti_2O_7}$, x=2.

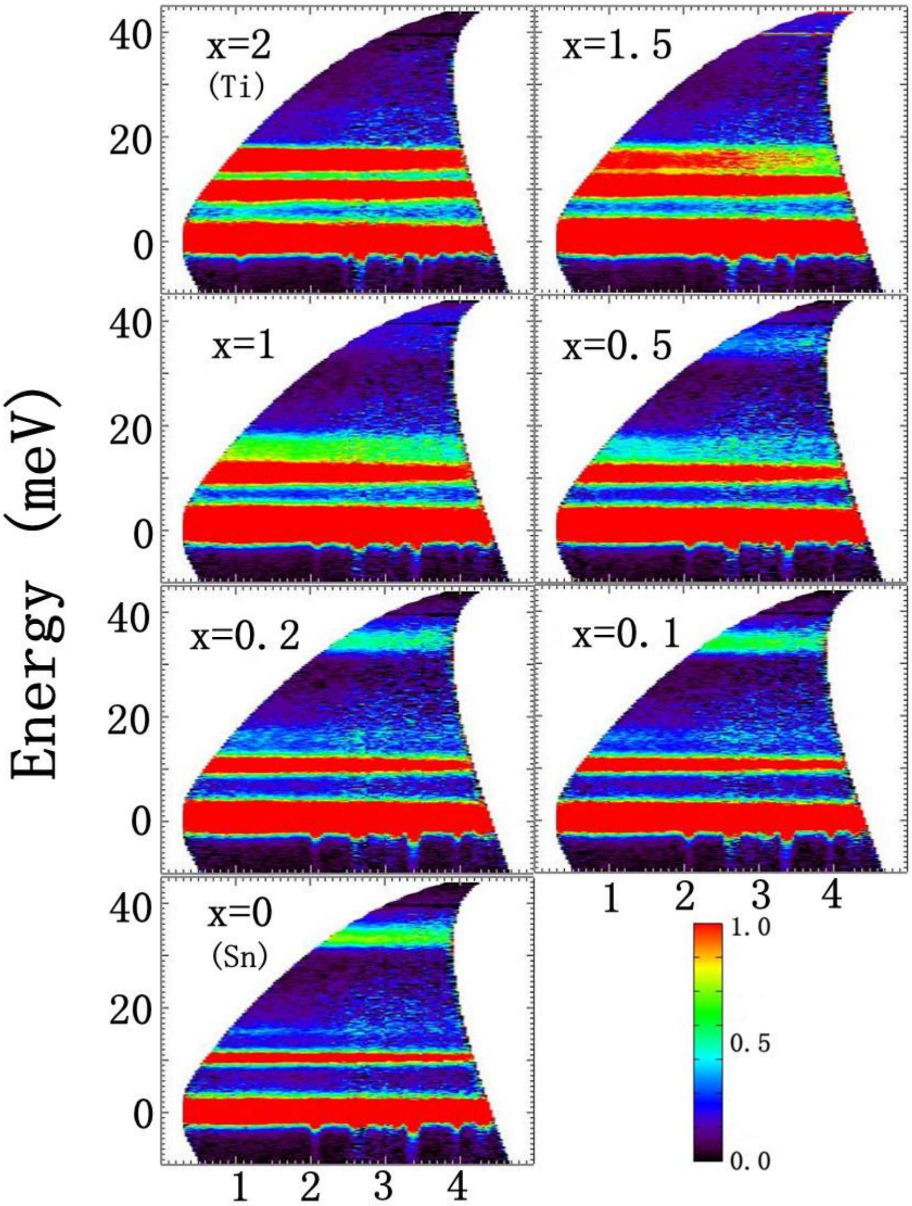

Figure 4.3: Color contour plots of the inelastic neutron scattering data for 7 concentrations of $Tb_2Sn_{2-x}Ti_xO_7$ at T=1.5K with E_i=45meV neutrons are shown.

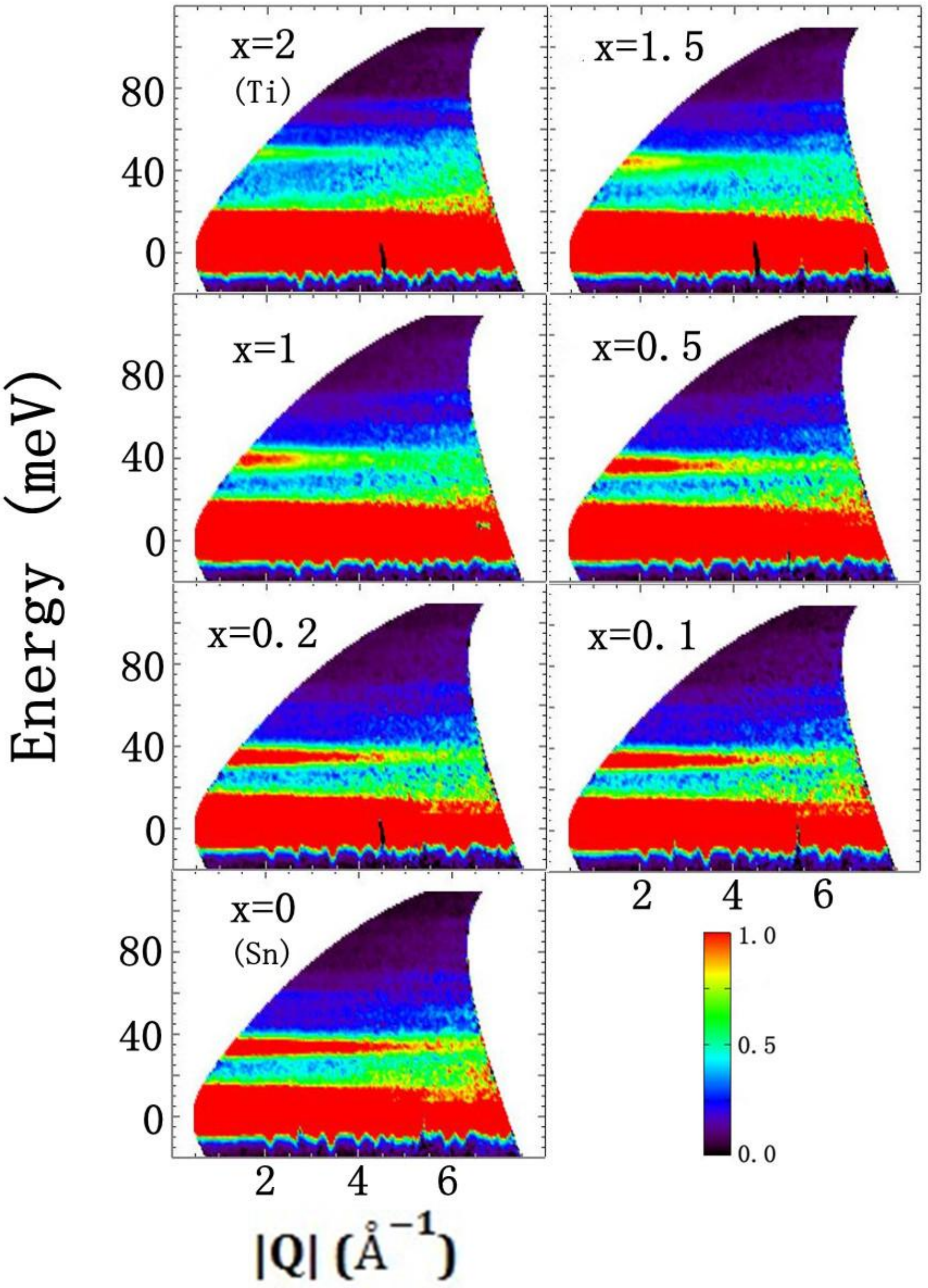

Figure 4.4: Color contour plots of the inelastic neutron scattering data for 7 concentrations of $Tb_2Sn_{2-x}Ti_xO_7$ at T=1.5 K with E_i=120 meV neutrons are shown.

first excited state doublet to the ground state doublet can be seen as sharp peaks around -1.5 meV for $\mathrm{Tb_2Ti_2O_7}$ and $\mathrm{Tb_2Sn_2O_7}$.

Next, in order to investigate the doping evolution of high energy crystal field excitations, another two experiments with higher incident neutron energies and over larger energy ranges were performed. Figures 4.3 and 4.4 show color contour maps of the inelastic neutron scattering data for the same 7 concentrations of $\mathrm{Tb_2Sn_{2-x}Ti_xO_7}$ taken with $\mathrm{E_i}$=45 meV and $\mathrm{E_i}$=120 meV neutrons respectively at T=1.5 K. In Figure 4.3, we observe obvious excitations as sharp peaks at around 10 meV for all 7 samples. More interesting excitations occur at around 15 meV. From x=0 to x=2, this excitation gradually changes from weak to strong and broad. In Figure 4.4, we observe higher energy excitations at around 40 meV for all 7 samples. From x=0 to x=2, this excitation gradually changes from a lower energy and a higher intensity mode to a higher energy and a lower intensity mode.

The color contour maps of the inelastic neutron scattering data can only give us a qualitative description of the characteristics of the excitations. In order to examine the details, it is better to extract line scans of the intensity vs energy for the data sets in Figures 4.1, 4.3 and 4.4 corresponding to each of the three $\mathrm{E_i}$s and for all seven samples at T=1.5 K. Doing so requires an integration of the data in |Q|, which depends on the energy range of interest. This is what is shown in Figure 4.5 A for $\mathrm{E_i} = 11\,\mathrm{meV}$, B for $\mathrm{E_i} = 45\,\mathrm{meV}$ and C for $\mathrm{E_i} = 120\,\mathrm{meV}$, wherein the intensity scales in Figure 4.5 A and B are logarithmic, while the intensity scale in Figure 4.5 C is linear.

At the lower energy, the intensity is integrated in |Q| between 1 $\mathrm{Å^{-1}}$ and 1.4 $\mathrm{Å^{-1}}$ in Figure 4.5A. We can observe similar features to those in Figure 4.1. For the two end members, x=0 and x=2, the well defined crystal field excitations are observed between the ground state doublet and the first excited state doublet near 1.5 meV. Instead, for the intermediate concentrations x=0.5, 1 and 1.5, no sharp transitions are observed and the spectral weight of the diffuse scattering in the regime of the lowest crystal field excitation is now extended to about 6 meV. On the other hand, compared with the two end member, we can see a much enhanced quasi-elastic scattering at low energies (<0.8 meV) in x=0.5, 1 and 1.5. Both of the quasi-elastic scattering and the diffuse scattering indicates the mixing of low energy crystal levels and low lying spin dynamics for the intermediate concentrations which are consistent with a dynamic and highly fluctuating ground state, distinct from the two end members $\mathrm{Tb_2Ti_2O_7}$ and $\mathrm{Tb_2Sn_2O_7}$.

At higher energies, the intensity is integrated in |Q| between 1 $Å^{-1}$ and 1.4 $Å^{-1}$ for $\mathrm{E_i}$=45 meV in Figure 4.5B and the intensity is intergrated in |Q| between 2 $Å^{-1}$ and 3 $Å^{-1}$ for $\mathrm{E_i}$=120 meV in Figure 4.5C. Both of the two figures show a continuous evolution of the crystal field excitations with concentration. Therefore, we turn our attention to the doping dependence of the excitations. In Figure 4.5B, the intensities of the excitations at 10 meV and 16 meV gradually rise from one end x=0, $\mathrm{Tb_2Sn_2O_7}$ to the other end x=2, $\mathrm{Tb_2Ti_2O_7}$, and in the second excitation position at 16meV, the transition changes smoothly from one peak in x=0, $\mathrm{Tb_2Sn_2O_7}$ to two peaks in x=2, $\mathrm{Tb_2Ti_2O_7}$. At the highest energies studied in Figure 4.5C, we observe a remarkable electronic homogeneity in the disordered systems $\mathrm{Tb_2Sn_{2-x}Ti_xO_7}$, as the appropriate crystal field excitation evolves from about 32 meV for x=0, $\mathrm{Tb_2Sn_2O_7}$ to about 49 meV for x=2, $\mathrm{Tb_2Ti_2O_7}$, along with a decrease in the intensity of the excitation. In order to extract the crystal field excitation energies for all the seven concentrations, we fit the excitation peaks to Lorentzians, and obtained the excitation energy, E, as a function of concentration x, which is shown in the inset to Fig. 4.2C. Clearly we can see that the evolution of this high energy crystal field excitation is linear with composition. Furthermore, for the intermediate concentrations, instead of a

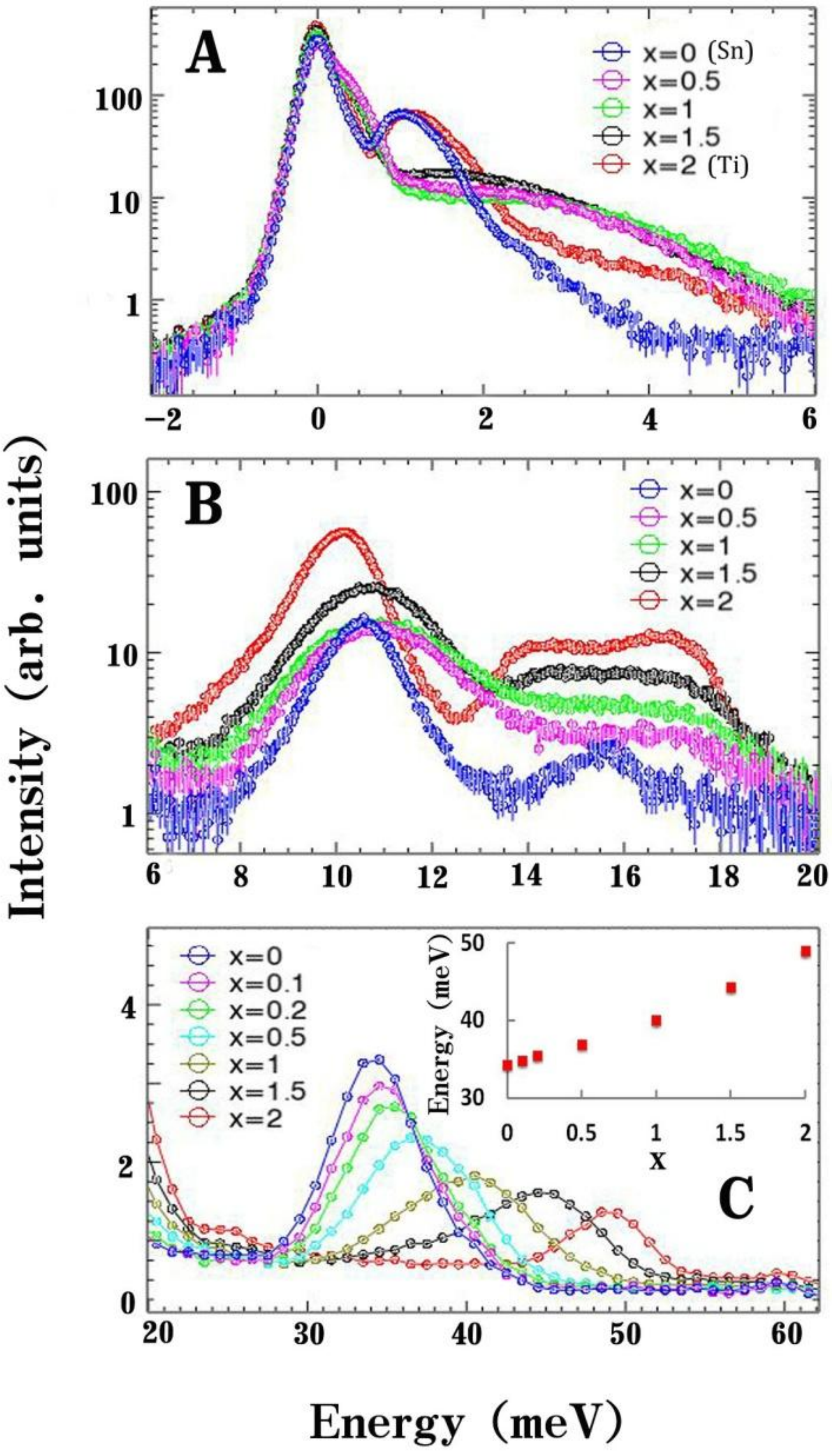

Figure 4.5: Cut plots of the inelastic neutron scattering data for

$Tb_2Sn_{2-x}Ti_xO_7$ samples taken at 1.5 K are shown. A and B show cuts of Figures 4.1 and 4.3 on a logarithmic intensity scale taken with E_i=11 meV and 45 meV neutrons, respectively. C shows cuts of Figures 4.4 on a linear intensity scale taken with E_i=120 meV neutrons. Intensities in A and B have been integrated between 1 $Å^{-1}$ and 1.4 $Å^{-1}$, while that in C has been integrated between 2 $Å^{-1}$ and 3 $Å^{-1}$ in |Q|. The high energy CF excitations in C were fit to Lorentzians and their energies are plotted as a function of x in the inset to C.

coexistence of the low energy crystal field levels, the excitations remain well defined, distinct from the two end members, although the crystal field excitation broadens somewhat. This shows an unexpected high degree of homogeneity at these high energies. These features are consistent with those in Figures 4.3 and 4.4.

4.3 AC Magnetic Susceptibility Measurements

In the rest of this chapter, the AC magnetic susceptibility data and the μSR data are provided by our experimental collaborators. I want to emphasize that these are not my own work.

In this section and next section, we will separately study this series of solid solutions $\mathrm{Tb_2Sn_{2-x}Ti_xO_7}$ using AC magnetic susceptibility and μSR experiments at lower temperatures to mainly study the phase behavior and low energy spin dynamics.

Figure 4.6 shows the real part χ', and imaginary part χ'' of the susceptibility measured as a function of temperature below 1 K with an intermediate frequency of 500 Hz in zero applied field in A and B, respectively to illustrate the variation among this same solid solutions $\mathrm{Tb_2Sn_{2-x}Ti_xO_7}$.

For x=0, $\mathrm{Tb_2Sn_2O_7}$, the peak in χ' and concomitant inflection in χ'' at T_N~0.83 K, indicating the transition to “soft” spin ice ordered phase. The transition temperature T_N is a little lower than previously reported (0.87 K) [4]. These features are wiped out for all subsequent levels of Sn/Ti mixing, including the most lightly disordered x=0.1 sample, indicating the fragility of the ordered phase in $\mathrm{Tb_2Sn_2O_7}$ [5]. For x=0.1, we observe two interesting features, one of which is the suppression of the magnetic ordering peak in χ' and the other is no sign of spin freezing out since there is no downturn in

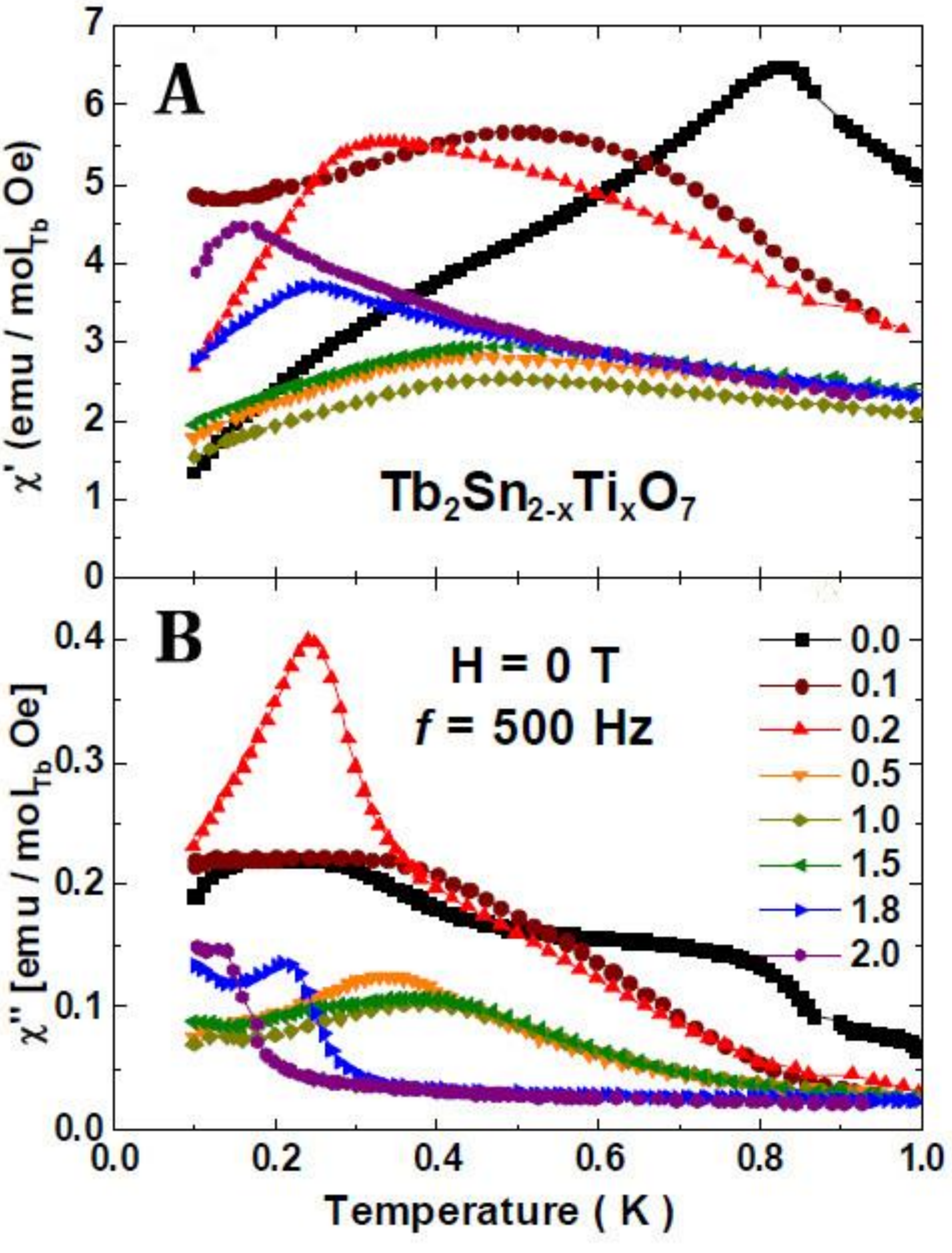

Figure 4.6: AC magnetic susceptibility measurements were performed in zero DC magnetic field, at a frequency of 500 Hz. A and B show the real, χ', and imaginary, χ'' parts of the AC susceptibility for $\mathrm{Tb_2Sn_{2-x}Ti_xO_7}$ at low temperatures < 1 K respectively.

either χ' or χ'' at low temperature limit.

At the other end of the solid solutions, the pure $Tb_2Ti_2O_7$, x=2 and most lightly disordered sample x=1.8, we observe weak peaks in both χ' and χ'' signifying glassy behavior for temperatures of ~0.23 K and below, consistent with earlier studies [6-9].

For the intermediate concentrations, in particular x=0.5, 1 and 1.5, we observe very broad and low absolute values curves for both χ' and χ'', again consistent with a disordered and strongly fluctuating ground state.

4.4 μSR Measurements

Figure 4.7 shows the longitudinal field μSR measurements on this same solid solution series $Tb_2Sn_{2-x}Ti_xO_7$ in a small longitudinal field H_L=50 Oe to decouple possible low field muon sites, spanning the temperature range from 20 mK to 300 K. We observe a nearly single exponential relaxation to the decay asymmetry in the whole temperature regime for all samples. The resulting relaxation rates as a function of temperature are shown in Fig. 4.7 A and B and we observe a gradual rising of the relaxation rate λ upon cooling and a level off at the lowest temperature measured.

For x=0, $Tb_2Sn_2O_7$ sample, the signature of the transition to the “soft” spin ice ordered phase is quite subtle in Fig. 4.7A and a weak inflection near T_N~0.9 K can be observed. A much more pronounced signature of T_N can be found in the difference of the relaxation rates measured after field cooling (FC) in an 800 Oe magnetic field and zero field cooling (ZFC) the x=0 sample in the inset of Fig. 4.4B. This FC-ZFC difference in the relaxation rate rises dramatically through T_N. However, this feature is rapidly suppressed for all subsequent levels of Sn/Ti mixing. We find that only a small 10% vestige of

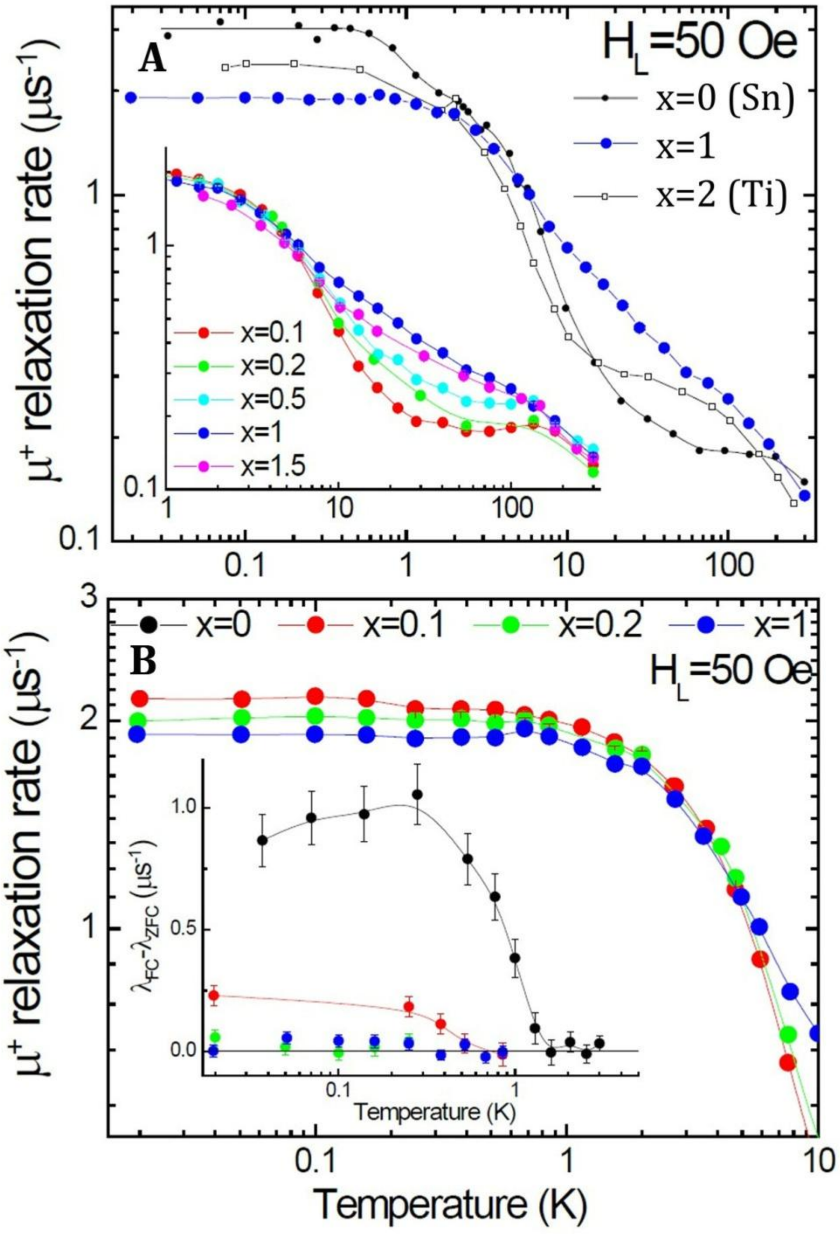

Figure 4.7: The μSR measurements were performed in a small 50 Oe longitudinal field. A and B show the μSR relaxation rate as a function of temperature for selected $Tb_2Sn_{2-x}Ti_xO_7$ samples. Both the relaxation rate and the temperature are plotted on logarithmic scales. The inset in B shows the difference between a field-cooled and zero field-cooled relaxation rate.

this anomaly survives even for lowest level of Sn/Ti mixing, x=0.1 and this signature has completely disappeared for x=0.2 and x=1, again indicating the fragility of the ordered spin ice state in $Tb_2Sn_2O_7$.

In Fig. 4.7A, both of the two end members $Tb_2Ti_2O_7$ and $Tb_2Sn_2O_7$ display a high temperature plateau between ~10 K and 200 K, due to the thermal occupation of the lowest lying crystal field excited states about 15 K above the ground state for either, while for the intermediate concentrations, the high temperature plateau fills in and becomes smooth evolution, due to the effect of the Sn/Ti mixing on the low lying crystal field levels, which is consistent with the disappearance of the well-defined lowest lying crystal field level at about 1.5 meV shown in Figs 4.1, 4.2 and 4.5.

Finally, let’s look at the relaxation rates at low temperature limit for different x values in Fig. 4.7A. For x=0, $Tb_2Sn_2O_7$, the relaxation rate reaches a plateau of ~3 μsec^{-1} at lowest temperatures measured and for x=2, $Tb_2Ti_2O_7$, it rises to ~2.5 μsec^{-1} at lowest temperatures measured, while for the intermediate concentrations, it gradually rises to a low temperatures limit of ~2 μsec^{-1}, a smaller value than the two end members, again confirming a very dynamic ground state.

4.5 Conclusion

From our inelastic neutron scattering, AC magnetic susceptibility and μSR experimental results, we observe a remarkable route to a new type of spin liquid state, based on disordered quantum spin ice. Since we know both the Sn^{4+} and Ti^{4+} sites are non-magnetic, we may naively expect the mixing of these two elements on the B-site of solid solutions of the form $Tb_2B_2O_7$ to have little effect on the low temperature physics displayed across the solid solution. Yet, it has a dramatic effect.

The mixing of $\mathrm{Sn^{4+}}$ and $\mathrm{Ti^{4+}}$ wipes out the subtle transition to a “soft” spin ice ordered phase in $\mathrm{Tb_2Sn_2O_7}$, showing the fragility of the ordered spin ice state. The intermediate concentrations show the disorder/mixing in the low lying $\mathrm{Tb^{3+}}$ crystal field environments but also show an unexpected high degree of homogeneity at high energy, indicating a very dynamic and highly fluctuating spin liquid ground state.

These results underline the crucial role played by the low lying excited CF doublet for $\mathrm{Tb^{3+}}$ in both end members, x=0 and x=2. The modification of the ground state and lowest excited state doublet wavefunctions on moving from x=0 to x=2, implies a disruptive change to the virtual excitations between the ground state and low lying excited states. As this is the mechanism proposed [10] by which quantum fluctuations are introduced to $\mathrm{Tb_2Ti_2O_7}$, and which presumably are also at play in $\mathrm{Tb_2Sn_2O_7}$, the advanced characterization of the $\mathrm{Tb_2Sn_{2-x}Ti_xO_7}$ solid solutions provides a unique and important perspective on such quantum fluctuations in the presence of relevant disorder

Bibliography

1. I. Mirebeau, P. Bonville, M. Hennion, Phys. Rev. B **76**, 184436 (2007)
2. J. Gardner, *et al.*, Phys. Rev. Lett. **82**, 1012 (1999)
3. J. Gardner, *et al.*, Phys. Rev. B **64**, 224416 (2001)
4. I. Mirebeau, *et al.*, Phys. Rev. Lett. **94**, 246402 (2005)
5. M. Dahlberg, M. Matthews, P. Jiramongkolchai, R. Cava, P. Schiffer, Phys. Rev. B **83**, 140410 (2011)
6. N. Hamaguchi, T. Matsushita, N. Wada, Y. Yasui, M. Sato, Phys. Rev. B **69**, 132413 (2004)
7. Y. Yasui, *et al.*, Journal of the Physical Society of Japan **71**, 599 (2002)
8. J. S. Gardner, *et al.*, Phys. Rev. B **68**, 180401 (2003)
9. E. Lhotel, *et al.*, Phys. Rev. B **86**, 020410 (2012)
10. Y. Kao, M. Enjalran, A. Del Maestro, H. Molavian, M. Gingras, Phys. Rev. B **68**, 172407 (2003)

Chapter 5

Conclusions

In this thesis, we have determined the eigenvalues and eigenfunctions appropriate to the (2J+1)=13 crystal field states appropriate to the J=6 Tb^{3+} magnetic moments in $\mathrm{Tb_2Sn_2O_7}$ and $\mathrm{Tb_2Ti_2O_7}$ by fitting our new time-of-flight inelastic neutron scattering data to the results of appropriate crystal field calculations. These results show the overall scale of the energy eigenvalues to be remarkable factor of ~2 greater in $\mathrm{Tb_2Ti_2O_7}$ compared with $\mathrm{Tb_2Sn_2O_7}$. This is consistent with the fact that the cubic pyrochlore lattice is strongly expanded in $\mathrm{Tb_2Sn_2O_7}$ compared with $\mathrm{Tb_2Ti_2O_7}$. For $\mathrm{Tb_2}Sn_2\mathrm{O_7}$, the ground state doublet is primarily $\mathrm{J_z} = |\mp 5>$, while the first excited state doublet is primarily $\mathrm{J_z} = |\mp 4>$. For $\mathrm{Tb_2Ti_2O_7}$, the ground state and first excited state doublets are made of a more equitable mixture of the symmetry allowed $\mathrm{J_z}$ basis states, but the largest component remains $\mathrm{J_z} = |\mp 5>$ for the ground state and $\mathrm{J_z} = |\pm 4>$ for the first excited state doublets.

Both of $\mathrm{Tb_2Sn_2O_7}$ and $\mathrm{Tb_2Ti_2O_7}$ belong to a family of geometrically frustrated cubic pyrochlore magnets, and display related, but different exotic ground states due to the interplay of magnetic interactions and anisotropies which they display. Nonetheless, both materials exhibit a variant of the spin ice ground state at sufficiently low temperatures, with $\mathrm{Tb_2Sn_2O_7}$ displaying “soft” spin ice order below ~0.87 K, while $\mathrm{Tb_2Ti_2O_7}$ shows a disordered, frozen antiferromagnetic spin ice state below ~0.2 K. This is consistent with the similarities between their structures, low lying crystal field states, and their interactions as quantified through their Θ_{CW}.

We have also presented a series of inelastic neutron scattering experiments, as well as accompanying AC magnetic susceptibility and μSR experiments performed by our collaborators to characterize the low temperature magnetic properties of $Tb_2Sn_{2-x}Ti_xO_7$ for seven different x values from one end x=0, $Tb_2Sn_2O_7$ to the other end x=2, $Tb_2Ti_2O_7$. We have studied the doping dependence of $Tb_2Sn_{2-x}Ti_xO_7$ to probe the crystal field states, low energy spin dynamics and phase transitions of these samples. The AC magnetic susceptibility and μSR measurements show that the magnetic order in x=0, $Tb_2Sn_2O_7$ is quite delicate and absent even for x=0.1. The AC magnetic susceptibility measurements also show glassy behavior in x=1.8 and x=2, $Tb_2Ti_2O_7$ below ~0.23 K. The inelastic neutron scattering measurements show a mixing of low lying crystal field levels for intermediate concentrations but a remarkable electronic homogeneity at high crystal field energies for all x in $Tb_2Sn_{2-x}Ti_xO_7$. All the three experiments reveal a greatly enhanced spin dynamics at low energies for the intermediate concentrations indicating a novel, dynamic spin liquid state for all x other than the two end members x=0, $Tb_2Sn_2O_7$ and x=2, $Tb_2Ti_2O_7$.